

**Identification of genetic risk variants for atherosclerosis using
oxidative stress assays in vascular smooth muscle cells and
bioinformatic approaches**

*Identifikation genetischer Risikovarianten für Artherosklerose via
oxidativem Stress Assay in glatten Muskulaturzellen und
bioinformatische Ansätze*

Masterarbeit

verfasst am
Institut für Kardiogenetik

im Rahmen des Studiengangs
Molecular Life Science
der Universität zu Lübeck

vorgelegt von
Torben Falk

ausgegeben und betreut von
Prof. Dr. Jeanette Erdmann

mit Unterstützung von
Dr. Tobias Reinberger

Lübeck, den 21. Juli 2022

Eidesstattliche Erklärung

Ich erkläre hiermit an Eides statt, dass ich diese Arbeit selbständig verfasst und keine anderen als die angegebenen Quellen und Hilfsmittel benutzt habe.

Torben Falk

Zusammenfassung

Ich muss das Ding wohl irgendwann auch noch in Deutsch schreiben...

Abstract

Placeholder

Acknowledgements

Daaanke an alle!

Contents

1	Introduction	1
1.1	Coronary artery disease	1
1.2	VSMCs in CAD	1
1.3	transforming Growth Factor beta (TGF β) Signaling	2
1.4	PDGF Signaling	2
1.5	GWAS	3
1.6	Complementary High Through Put Methods	5
1.7	Aim of the thesis	7
2	Material	8
2.1	Manufactors	8
2.2	Celllines	9
2.3	Primer	9
2.4	Chemicals	10
2.5	Media, Supplements	11
2.6	Solutions	11
2.7	Kits	11
2.8	Consumables	11
2.9	Devices	12
2.10	Programs & Modules	13
3	Methods	15
3.1	Cultivation and differentiation of HAoSMCs	15
3.2	mRNA Quantification	16
3.3	Energy Profiling	18
3.4	Oxidative Stress Assay	19
3.5	Curation of Data for postGWAS Analyses	21
3.6	Visualization of GWAS data	22
3.7	Enrichment analysis	23
4	Results	26
4.1	Differentitaion	26
4.2	Evaluation of oxidative Stress	30
4.3	Database and GWAS Visualizer	34
4.4	Enrichment analysis	37

5	Discussion	40
5.1	PDGF-BB Signaling Seems to Induce a Synthetic Phenotype in HAoSMCs .	40
5.2	CellROX™ Green is Suitable for Assessing ROS Generation in HAoSMCs .	41
5.3	The GWAS Navigator	42
5.4	Overlap of CAD Associated Variants with Regulatory Elements is Enriched in Heart, Artery & Lung Tissue	43
	Bibliography	50

1

Introduction

1.1 Coronary artery disease

Coronary artery disease (CAD) is among the leading causes of death in the (western) world-wide, being prevalent in about 6.7% of American adults and killing more than 350'000 people in the USA in 2019 alone (Disease Control and Prevention, 2022; Fryar, 2012). CAD is characterized by the build-up of fatty plaques in the arteries leading to the heart. This process called atherosclerosis can interrupt the blood supply to the heart (National Health Service, 2017). Its most common complication is myocardial infarction (MI) which usually manifests as chest pain (angina) and can cause serious damage to the heart muscle. Long time, CAD can lead to heart failure (HF), the hearts inability to properly pump the blood. Next to common and well-known lifestyle factors like tobacco use or physical inactivity, CAD risk additionally has a hereditary component (Montalescot et al., 2013).

1.2 VSMCs in CAD

The lumen of a typical blood vessel is surrounded by three distinct layers. The outer adventitia is rich in connective tissue, shapes the vessel, and wraps the media. The media contains vascular smooth muscle cells (VSMCs) which are required to mediate vasodilation and vasoconstriction according to signaled requirements. The inner layer consists of endothelial cells that define the lumen of the vessel. (Tucker et al., 2022; Yap et al., 2021) For the longest time, the role of VSMCs in the development and progression of atherosclerosis has been underestimated and over-simplified. VSMCs have simply been considered to be either promoting arteriosclerosis or beneficial for plaque stability. Only with the emergence of novel and exciting technologies like single-cell (sc) transcriptomics and lineage tracking, this model is changing into a more multifaceted one. (Liu and Gomez, 2019; Grootaert and Bennett, 2021; Yap et al., 2021) The study of VSMCs in arteriosclerosis is rapidly evolving, and the underlying models being adjusted accordingly. The black and white idea of VSMCs in arteriosclerosis existing either as a differentiated (contractile) phenotype or as a dedifferentiated (synthetic) phenotype, is making place for a model that considers a diverse set of dedifferentiated phenotypes (Liu and Gomez, 2019; Grootaert and Bennett, 2021; Yap et al., 2021). The phenotypic switch describes the down-regulation of contractile markers and can give rise to a diverse bouquet of different phenotypes which can be found

in the fibrous cap and plaque core (Grootaert and Bennett, 2021). The characterization of these dedifferentiated phenotypes, as well as their impact on disease progression, are still the subject of intensive research.

Two external stimuli that seem to play central roles as cytokines determining the fate of VSMCs in atherogenesis are transforming Growth Factor beta ($\text{TGF}\beta$) & platelet-derived growth factor-BB (PDGF-BB).

1.3 $\text{TGF}\beta$ Signaling

$\text{TGF}\beta$ Signaling in General

The term $\text{TGF}\beta$ describes a superfamily of cytokines, the most prominent of which is $\text{TGF}\beta 1$. After secretion and activation, the active $\text{TGF}\beta$ dimer binds to a heteromeric receptor complex. The intracellular signaling is mainly implemented via Smad transcription factors. The effects of $\text{TGF}\beta$ are highly dependent on the cell type, and can even be pleiotropic for cells of the same type. The most prominent function of $\text{TGF}\beta$ is its role in the anti-inflammatory regulation of immune cells. (Goumans and Dijke, 2018; Batlle and Massagué, 2019)

$\text{TGF}\beta$ Signaling in VSMCs & atherosclerosis

In the context of VSMCs, $\text{TGF}\beta$ promotes proliferation and hypertrophy. Further, it promotes VSMC differentiation, via elevation of contractile gene expression as well as the down regulation of Kruppel-like factor 4 (KLF4) (Davis-Dusenbery et al., 2011), a transcription factor (TF) prominent for its application in inducing pluripotency (Takahashi et al., 2007) that is also required for phenotype switching. This way hindering (Davis-Dusenbery et al., 2011) or potentially reversing phenotype switching (Pan et al., 2020).

1.4 PDGF Signaling

PDGF Signaling in General

Five different platelet-derived growth (PDGF) isoforms (PDGF-AA, PDGF-AB, PDGF-BB, PDGF-CC & PDGF-DD) have been identified that are formed as dimeric combination of four distinct polypeptide chains. All five isoforms bind to tyrosine kinase receptors (platelet-derived growth factor receptor ($\text{PDGFR}\alpha$ & $\text{PDGFR}\beta$). Upon activation, the receptor dimerizes, allowing autophosphorylation which activates the kinase domain and creates binding sites for signaling molecules. The active receptor is involved in a plethora of prominent messaging pathways like the mitogen activated protein (MAP)-kinase pathway, phosphatidylinositol 3'-kinase (PI3K)-signaling or signal transducers and activators of transcription (STAT)-signaling. All these pathways are ultimately involved in the promotion of cellular proliferation, survival and migration (Chen et al., 2013; Heldin, 2013; Hu and Huang, 2015).

The predominantly expressed isoforms of endothelial cells seems to be PDGF-BB (Andrae et al., 2008; Heldin, 2013) which acts as a paracrine activator for VSMCs and other mesenchymal cells (Heldin, 2013). Signaling via PDGF-BB and the $\text{PDGFR}\beta$ plays an

important role in development of multiple tissues, amongst other in the development of the cardio vascular system (Levéen et al., 1994). In the adult, PDGF-BB picks up an important role in wound healing processes (Robson et al., 1992). The role of PDGFR β signaling in pathologic processes like cancer or cardio vascular disease has been a subject of extensive study for decades (Heldin, 2013; Raines, 2004).

PDGF Signaling in VSMCs & atherosclerosis

In the context of VSMCs, PDGF-BB was shown to increase KLF4 levels, which results in up-regulation of mesenchymal markers as well as the loss of contractile markers. Ultimately, serving as an external stimulus for proliferation and phenotype switching (Yap et al., 2021). Similarly to the overall role of VSMCs in arteriosclerosis, the role of PDGF-BB is still the subject of extensive study. All PDGF isoforms are abundantly found in arteriosclerotic cell walls, further PDGFR expression is elevated in affected vessels (Hu and Huang, 2015). For a long time PDGF signaling and inflammation has been assumed to be disease promoting (Andrae et al., 2008; Chen et al., 2013; Hu and Huang, 2015) and in 2015 He et al. (2015) showed that PDGFR β signaling in mouse model leads to inflammation and increased plaque formation. In contrast to this consensus, Newman et al. (2021a) were recently able to demonstrate, that sustained signaling via PDGFR β is required for VSMC involvement in arteriosclerotic lesions. They Further observed (again in mouse model) that lack of VSMC involvement during plaque formation, can be temporarily compensated by non-VSMC-derived cells, but long-term leads to instability of arteriosclerotic lesions.

ROS in PDGF Signaling

Reactive oxygen species (ROS) is a broad term for a class of highly reactive molecules derived from elemental oxygen (O_2). They are traditionally infamous for the damage they can do to proteins and nucleic acids when not kept in check, potentially causing irreparable damage and ultimately leading to cell death. Recently, this perception has been shifting, and especially hydrogen peroxide (H_2O_2) and superoxide anion radical ($O_2^{\bullet-}$), are being recognized for their role in cellular signaling. (Sies and Jones, 2020)

Human cells contain dozens of enzymes, which are capable of generating ROS and enzymatically maintain a steady redox state (Sies and Jones, 2020). H_2O_2 and $O_2^{\bullet-}$ serve as important second messengers in the central nervous system (Nayernia et al., 2014) or in the repair of vascular lesions (Andrae et al., 2008). Interestingly, the generation of ROS as a second messenger gets triggered by stimulation with PDGF-BB (Sundaresan et al., 1995; Bouzigues et al., 2014).

1.5 GWAS

The hereditary components of disease onset and progression can provide access to its pathology on a molecular level.

GWAS

An amazing resource for getting a first glance into these interactions are genome wide association study (GWAS), a method that allows for the identification of genetic variants

associated with a phenotype.

While GWAS were initially an extraordinary endeavor, requiring the evaluation of hundreds or thousands of participants, they have gotten a lot more accessible with the availability of genetic data from public biobanks. After profiling the cohort on a genomic level (today usually via microarrays, in the future most likely via whole genome sequencing (WGS)) and phenotypically, the collected data needs to pass through several steps of quality control, e.g. for the removal of rare variants, miss-matched phenotypes, etc. Afterward, variants that were not directly analyzed are inferred from a reference. The final step of the initial analysis is the statistical model, a regression model that is used to test for the association of all variants with the phenotype in question. It is crucial to be completely aware of potential biases, some of which (like age, sex, or ancestry) can and need to be included as covariants in the used model. (Uffelmann et al., 2021; Flint, 2013) The model will output a list of p-values, effect sizes (and their direction) for all tested variants. A GWAS is the first important step in determining causal variants for disease and therefore a first glimpse into the molecular biology of the observed phenotype (Uffelmann et al., 2021).

postGWAS

Unfortunately, GWAS are just the first step in a long journey of establishing causal loci to gene links, uncovering the molecular basis of disease, and implementing tools for clinical risk prediction. A plethora of follow-up analyses (postGWAS) can and need to be performed to determine a set of credible variants and to assess their molecular mechanism.

The first important follow-up is fine-mapping. Due to the complex linkage disequilibrium (LD) of variants in the human genome (see section 1.6), loci identified in GWAS usually do not contain a single variant but form a potentially large set of linked and significant variants. Fine-mapping describes the process of identifying the actual causal variant in this mess. Multiple sophisticated statistical methods have been developed, the most popular of which is Bayesian modeling, which outputs variant-specific posterior inclusion probabilities (PIPs) that form a credible set of potentially causal variants. It is important to remember that methods for fine-mapping are still continuously refined and will most likely keep getting better and more complex with the increasing complexity of the studied phenotypes. Further, fine-mapping is a statistical approach that will never be able to determine causality! (Schaid et al., 2018; Uffelmann et al., 2021)

After the identification of likely causal variants, the next steps aim to gain information on their effect in determining the analyzed phenotype. Variants require mapping to impacted genes, associated pathways, and relevant tissues to get a glance at the complete picture. For these steps, no standard protocols exist and the procedure highly depends on the genomic context of the individual variant. Coding variants are rare but offer themselves to be immediately studied on a protein level, while non-coding variants usually greatly benefit from the consultation of more high throughput data in the form of e.g. expression quantitative trait loci (eQTL) (Uffelmann et al., 2021).

Finally, the results and ideas derived from statistical models can and need to be taken back to the wet lab, to be extended and verified. Utilizing all the recent great advances in molecular and cellular biology such as the development of increasingly comprehensive *in vitro* models as well as their manipulation via methods like clustered regularly interspaced short palindromic repeats (CRISPR)-Cas gene-editing (Lichou and Trynka, 2020).

1.6 Complementary High Through Put Methods

The development of high through put methods as well as the great increase in computing power over the last few years have spawned a plethora of incredible datasets that already have been and can be further utilized for postGWAS analyses. A short overview of some definitions and methods mentioned in this thesis can be found in the following paragraphs:

Linkage Disequilibrium

LD is a parameter from populations genetics that describes the non-random association of two or more alleles. The LD is often quantified using the correlation coefficient r^2 (Slatkin, 2008).

$$D_{AB} = p_{AB} - p_A p_B$$

$$r^2 = \frac{D_{AB}^2}{p_A(1 - p_A) \times p_B(1 - p_B)}$$

Where p_A and p_B are the frequency of the alleles A and B respectively. p_{AB} is the frequency of the AB haplotype.

The LD becomes important in the context of GWAS because identified SNPs often do not occur in isolation, but as a network of linked and significant variants that can span large haplotype blocks in the genome (Slatkin, 2008).

Locus To Gene Scores

Problems of interpretation of GWAS data are already described in section 1.5. Link to gene (L2G) scores are an attempt at overcoming the challenges of establishing causal relationships between variants and genes. The authors employed a machine learning model to integrate fine-mapping with functional genomics data and *in silico* predictions to link GWAS loci to their target genes. The output L2G scores are calibrated to represent the probability (0, 1). (Mountjoy et al., 2021)

Regulatory Build

The Ensembl Regulatory Build compiles a summary of putative regulatory regions found in the (human) genome. It is constructed from publically available data on epigenetic marks and TF binding sites. It contains promoters, proximal enhancers, distal enhancers, and CCCTC binding factor (CTCF) binding sites. (Zerbino et al., 2015)

ENCODE cCRE

Very similarly, the ENCyclopedia Of DNA Elements project (ENCODE) project summarizes deoxyribonucleic acid (DNA) accessibility and chromatin modification data into candidate cis-regulatory elements (cCREs). Regions showing high DNase signal are further

annotated to be proximal enhancer-like elements (pELS) or distal enhancer-like elements (dELS), promoter-like elements (PLS), other regions with high histone 3 lysine 4 trimethylation (H3K4me3) signal (which might represent poised or non-canonical promoters), or CTCF-only elements based on the existence of H3K4me3, histone 3 lysine 27 acetylation (H3K27ac), or CTCF marks. (Moore et al., 2020)

ATAC-seq

Assay for transposase-accessible chromatin using sequencing (ATAC-seq) is a method to access chromatin accessibility in the genome. ATAC-seq utilizes the hyperactive Tn5 transposase to insert sequencing adapters into accessible regions of chromatin. DNA is purified and amplified via polymerase chain reaction (PCR) and then sequenced. Mapping sites with insertions in the genome allows for the identification of highly accessible genomic regions. (Buenrostro et al., 2013; Buenrostro et al., 2015a)

PCR amplification of the DNA makes this method extremely sensitive. Pushing the requirement of biomaterial to the minimum, ATAC-seq is applicable on a single-cell level. For scATAC-seq, individual cells are isolated, and their DNA tagged with barcoded primers during the PCR. These barcodes allow mapping of ATAC-seq data to the isolated cells. (Buenrostro et al., 2015b)

ABC Model

The activity by contact (ABC) model grants insights into potential cell specific enhancer-gene interactions based on chromatin state, outperforming previously used methods (Fulco et al., 2019; Nasser et al., 2021).

$$ABC\ score_{E,G} = \frac{A_E \times C_{E,G}}{\sum_{\text{all elements } e \text{ within } 5\text{ Mb of } G} A_e \times C_{e,G}}$$

Generally speaking, the model incorporates the activity of an enhancer A_E , as well as contacts with the gene of interest $C_{E,G}$, normalized by the total effect of all elements in proximity (Fulco et al., 2019; Nasser et al., 2021).

Hi-C & TADs

Hi-C is a method for mapping chromosomal conformation. To achieve this, genome-associated proteins are cross-linked with formaldehyde, the DNA is digested with restriction enzymes, and generated overhangs are filled in with biotinylated nucleotides. The resulting fragments are ligated, this way covalently linking DNA fragments, which were originally in close spatial proximity. The DNA is purified and fragmented allowing the pulldown of fragments containing junctions sites via the filled-in biotin tags. After sequencing the enriched fragments, their sequences are mapped to the genome, identifying interacting DNA regions. (Lieberman-Aiden et al., 2009; Wit and Laatz, 2012)

Looking at Hi-C data, TADs were identified to be a basic feature of genome organization with an average size of 880 kb (Dixon et al., 2012; Wang et al., 2018b). What makes TADs

of such high interest is the fact that interactions of DNA sequences are usually confined within TADs. Tissue-specific genes and their enhancers are usually found in the middle of TADs, while the edges enrich for housekeeping genes and CTCF binding sites, which might serve as insulators between different domains (Pombo and Dillon, 2015).

1.7 Aim of the thesis

The aims of this thesis are split into two quite distinct projects that both ultimately aim to contribute to a better understanding of arteriosclerosis and CAD:

- The split role of PDGF-BB during progression of arteriosclerosis (see section 1.4), indicates that PDGF-BB signaling is neither completely beneficial nor disadvantageous to diseases, but there is an optimal dosage of stimulation. Combining this theory with the fact that ROS are involved in PDGF-BB signaling and also highly associated with arteriosclerosis (Burtenshaw et al., 2019), we hypothesized, that PDGF-BB signaling may cause oxidative stress, this way contributing to disease progression. The first part of this thesis will deal with the *in vitro* characterization of PDGF-BB stimulated VSMCs and the establishment of a robust assay for oxidative stress in VSMCs.
- As most data is generated by high-throughput methods, the summary statistics from Aragam et al. (2021) are a great resource. One of the goals of this thesis is to make this data and its context easily accessible to medical researchers in the form of an interactive web-based visualization tool. The GWAS Navigator will co-visualizing GWAS summary statistics with different annotations in the form of gene products, associated phenotypes from other GWAS or putative regulatory elements.
- Finally, the data curated for the GWAS Navigator will be used in an enrichment analysis, checking different biosamples for the overlap of disease-associated variants with regulatory elements.

Have fun with my thesis, this still is a mess...

2

Material

2.1 Manufacturers

Manufacturer	Seat
Agilent Technologies, Inc.	Santa Clara, CA, USA
Glaswarenfabrik Karl Hecht GmbH & Co. KG	Sondheim vor der Rhön, DE
Brand GmbH & Co. KG	Wertheim, DE
ChemoMetec A/S	Allerød, DK
Eppendorf SE	Hamburg, DE
Heraeus Holding GmbH	Hanau, DE
Merck KGaA	Darmstadt, DE
Keyence Corporation	Osaka, JP
Kisker Biotech GmbH & Co. KG	Steinfurt, DE
Sarstedt AG & Co.	Nürnberg, DE
Sigma-Aldrich Co. LLC.	St. Louis, MO, USA
Thermo Fisher Scientific Inc.	Waltham, MA, USA
PeproTech© (Brand of Thermo Fisher Scientific Inc.)	Hamburg, DE
Pechiney Plastic Packaging, Inc.	Chicago, IL, USA
J.T.Baker® (Brand of Thermo Fisher Scientific Inc.)	Schwerte, DE
GFL mbH	Burgwedel, DE
Applied Biosystems (Brand of LUMITOS AG)	Warrington, UK

Continued on next page

(Continued)

Manufacturer	Seat
Gibco BRL (Brand of Thermo Fisher Scientific Inc.)	Gaithersburg, MD, USA
ibidi GmbH	Gräfelfing, DE
Invitrogen™AG (Brand of Thermo Fisher Scientific Inc.)	Schwerte, DE
Lonza Group AG	Basel, CHE
Bio&SELL GmbH	Feucht, DE
New England Biolabs GmbH	Ipswich, MA, USA
Nikon Corporation	Minato, JP
Sartorius AG	Göttingen, DE
SensoQuest GmbH	Göttingen, DE
Hanna Instruments Deutschland GmbH	Vöhringen, DE
Heidolph Instruments Labortechnik	Schwabach, DE
ZIEGRA Eismaschinen GmbH	Isernhagen, DE
Mettler-Toledo GmbH	Gießen, DE
Serif (Europe) Ltd.	Nottingham, UK
Microsoft Deutschland GmbH	München, DE
GitHub, Inc. (Part of Microsoft Corporation)	San Francisco, CA, USA
Python Software Foundation	Beaverton, OR, USA
JetBrains s.r.o.	Prague, CZ
The SQLite Consortium (Contact via Hipp, Wyrick & Company)	Charlotte, NC, USA

2.2 Celllines

Name	Celltype	Manufacturer
Human Aortic Smooth Muscle Cell (HAoSMC)	prim. human cell	!?

2.3 Primer

Target	Name	Sequence
CNN1	Fw	5'-seq-3'
	Rv	5'-seq-3'
GAPDH	Fw	5'-seq-3'
	Rv	5'-seq-3'
MMP9	Fw	5'-seq-3'
	Rv	5'-seq-3'

2.4 Chemicals

Name	Manufacturer
5X First Strand Buffer	Invitrogen™ AG
Antimycin A	Sigma-Aldrich Co. LLC.
BSA	!?!?
CellROX™ Green Reagent	Thermo Fisher Scientific Inc.
Collagen Type I, rat tail	ibidi GmbH
dNTP Mix	Applied Biosystems
DTT	Invitrogen™ AG
Ethanol (99.9 %)	J.T.Baker®
FCCP	Sigma-Aldrich Co. LLC.
D-(+)-Glucose, 45 % solution	Sigma-Aldrich Co. LLC.
GlutaMAX™-I	Gibco BRL
Hoechst 33342,	Invitrogen™ AG
IL-1 β	PeptoTech©
M-MLV RT (200 U/ μ L)	Invitrogen™ AG
NAC	Sigma-Aldrich Co. LLC.
NaHCO ₃	Carl Roth GmbH + Co. KG
NaOH, 1 N	Carl Roth GmbH + Co. KG
Oligomycin	Sigma-Aldrich Co. LLC.
Roth Hexanukleotid Random-Primer	Carl Roth GmbH + Co. KG
PBS	Lonza Group AG
PDGF-BB	PeptoTech©
Sodium Pyruvate (100 mM)	Gibco BRL
RiboLock RNase Inhibitor (40 U/ μ L)	Thermo Fisher Scientific Inc.

Continued on next page

(Continued)

Name	Manufacturer
Seahorse XF calibrant	Agilent Technologies, Inc.
PowerUp™SYBR™GREEN Master Mix	Thermo Fisher Scientific Inc.
TGF β	PeproTech©

2.5 Media, Supplements

Name	Manufacturer
FBS Gold Plus	Bio&SELL GmbH
Medium 231	Gibco BRL
Smooth Muscle Cell Growth Supplement	!?!?
XF Base Medium	Agilent Technologies, Inc.

2.6 Solutions

Name	Manufacturer
IL-1 β	10 μ g/mL IL-1 β 0.1 % BSA in PBS
NAC	0.25 M NAC in water, ~pH 7
PDGF-BB	100 μ g/mL PDGF-BB 0.1 % BSA in PBS
TGF β	10 μ g/mL TGF β 0.1 % BSA in PBS

2.7 Kits

Kit	Manufacturer
Total RNA Purification Kit	Jena Bioscience GmbH

2.8 Consumables

Name	Manufacturer
Quali-PCR-Tubes 0,2 mL	Kisker Biotech GmbH & Co. KG
Quali-PCR-Tubes 0,5 mL	Kisker Biotech GmbH & Co. KG
SafeSeal Gefäß 1,5 mL	Sarstedt AG & Co.
SafeSeal Gefäß 1,5 mL	Sarstedt AG & Co.
SafeSeal Gefäß 5 mL	Sarstedt AG & Co.
Nunc Cell-Culture Treated Multidish 24	Thermo Fisher Scientific Inc.
Agilent Seahorse XF24 Cell Culture Microplate	Agilent Technologies, Inc.
Agilent Seahorse XF24 Extracellular Flux Assy Kit	Agilent Technologies, Inc.
384 Well Multiply PCR plates	???
Pasteurpipetten ISO 7712	Glaswarenfabrik Karl Hecht GmbH & Co. KG
Pipette tip 20 µL	Sarstedt AG & Co.
Pipette tip 200 µL	Sarstedt AG & Co.
Pipette tip 1000 µL	Sarstedt AG & Co.
Filter tip 20 µL	Sarstedt AG & Co.
Filter tip 200 µL	Sarstedt AG & Co.
Filter tip 1000 µL	Sarstedt AG & Co.
BD Discardit™ II	???
Spritzenfilter CHROMAFIL® PTFE, 0,20 µm	Carl Roth GmbH + Co. KG
Via1-Casette™	ChemoMetec A/S
Tube 15 ml	Sarstedt AG & Co.
Tube 50 ml	Sarstedt AG & Co.
Serological pipette 5 mL	Sarstedt AG & Co.
Serological pipette 10 mL	Sarstedt AG & Co.
Serological pipette 25 mL	Sarstedt AG & Co.
Serological pipette 50 mL	Sarstedt AG & Co.
Parafilm® M	Pechiney Plastic Packaging, Inc.
TC Flask T75, Cell+, Vented Cap	Sarstedt AG & Co.
CRYSTAL qPCR-Folie	New England Biolabs GmbH

2.9 Devices

Name	Manufacturer
Bench I Heraeus	Heraeus Holding GmbH
Bench II Heraeus	Heraeus Holding GmbH
Research pipettes (2.5 µL, 10 µL, 100 µL, 1000 µL)	Eppendorf SE
Hera Cell	Heraeus Holding GmbH
Hera Cell 150	Heraeus Holding GmbH
NucleoCounter NC-200	ChemoMetec A/S
Incubation/Inactivation bath 1083	GFL mbH
Centrifuge 5702 R	Eppendorf SE
Eclipse TS100	Nikon Corporation
Pipet-X	Mettler-Toledo GmbH
Centrifuge 5415 R	Eppendorf SE
Rotana 460 R	Andreas Hettich GmbH & Co. KG
XF24 Extracellular Flux Analyzer	Agilent Technologies, Inc.
7900HT Fast Real-Time PCR System	Thermo Fisher Scientific Inc.
LA 120 S	Sartorius AG
Reax Top	Heidolph Instruments Labortechnik
MR 3001	Heidolph Instruments Labortechnik
BZ-X810 All-in-One Fluorescence Microscope	Keyence Corporation
BZ-X800 All-in-One Fluorescence Microscope POWER	Keyence Corporation
SensoQuest labcycler	SensoQuest GmbH
pH 221 Microprocessor pH Meter	HANNA Instruments
NanoDrop™2000/2000c	Thermo Fisher Scientific Inc.
Spektralphotometer	
Eismaschine	ZIEGRA Eismaschinen GmbH

2.10 Programs & Modules

Programs

Program	Version	Manufacturer
Affinity Designer	1.10	Serif (Europe) Ltd.
Excel	Version 2205	Microsoft Corporation

Continued on next page

(Continued)

Program	Version	Manufacturer
GitHub	-	GitHub Inc
keyence software?!		Keyence Corporation
MiKTeX	2.9	Christian Schenk
python	3.9	Python Software Foundation
PyCharm (Community edition)	2021.2.2	JetBrains s.r.o.
SchemaSpy	5.0.0	John Currier
SDS	2.2.2	Thermo Fisher Scientific GmbH
sqlite3_analyzer	3.38.5.	The SQLite Consortium
Wave Controller	2.6.3	Agilent Technologies, Inc.

Python Modules

Module	Version	Info
beautifulsoup4	4.11.1	crummy.com/software/BeautifulSoup
bokeh	2.4.1	bokeh.org
numpy	1.21.4	numpy.org
pandas	1.3.4	pandas.pydata.org
Pillow	8.4.0	python-pillow.org
pylifter	0.4	github.com/konstantint/pylifter
python standard library	3.9	docs.python.org
matplotlib	3.4.3	matplotlib.org
requests	2.26.0	requests.readthedocs.io
scipy	1.7.3	scipy.org
seaborn	0.11.2	seaborn.pydata.org
urllib3	1.26.7	urllib3.readthedocs.io
wget	3.2	bitbucket.org/licface/pywget

Frameworks

- This thesis was generated with the [uzl-thesis class](#) kindly provided by Prof. Till Tantau.
- Styling of the GWAS Visualizer was done with the [cascading style sheets \(CSS\) Framework Bootstrap](#).

3

Methods

3.1 Cultivation and differentiation of HAoSMCs

For the following experiments, human aortic smooth muscle cells (HAoSMCs) were used. A cell type commonly used for the study of cardiovascular function and disease ([**Reference for this claim**]). Cells were kept at 37°C and 5 % carbon dioxide (CO₂) whenever possible. For differentiation, cells were at first treated with TGF β to induce a contractile phenotype and then further stimulated with interleukin 1 beta (IL-1 β) & PDGF-BB to induce a synthetic phenotype. For more information, please check the section 1.3 & 1.4 as well as the referenced literature.

Thawing & Cultivation

For longtime storage, cells were stored in liquid nitrogen. When required, new cells (6th passage) were thawed at 37°C in the water bath and transferred to a 15 mL tube. After centrifugation for 2 min at 300xg the supernatant was removed and the cell pellet was taken up in 14 mL of Human Vascular Smooth Muscle Cell Basal Medium (Medium 231) (M231) + SMGS for cultivation in a TC Flask T75. Every other day, 2/3 of the medium was removed and replaced by fresh. Cells were cultivated to a maximum passage of 10.

Passaging

When reaching a maximum of 80 % confluency (approx. once a week) the medium was removed completely and cells were washed once with 5 mL of PBS. The washed cells were incubated with 3 mL trypsin for 4 min at 37°C before 7 mL M231 were added to the detached cells. Further, the cell suspension was transferred to a 15 mL tube and pelleted for 4 min at 300xg. Finally, supernatant was removed and the pellet resuspended in M231 + SMGS, seeding 500×10^3 cells per TC Flask T75.

Preparation of Collagen I matrix

For preparation of the collagen type I (col I) matrix (1.8 mg/mL) all the components were mixed, adding the col I last. All components were stored at 4°C and all pipetting steps were carried out on ice:

Table 3.1: col I Matrix Composition

component	concentration	volume (μL)
H2O	-	38.9
M231	-	53.3
SMGS	20x	5,3
NaOH	1 M	2,7
NaHCO ₃	7.5 %	2.1
Col I	5 mg/mL	57.6
total	-	160

160 μL of matrix mix were transferred in each used well of a Nunc™ Cell-Culture Treated Multidish 24 (24 well multidish), fully coating the bottom of the wells. For polymerization, the matrix was incubated at 37°C for at least 60 min.

Differentiation of HAoSMCs

Differentiation was carried out over a total of 7 d in the 24 well multidish. 1 mL M231 was used as the medium, supplemented with 1 % FBS and different cytokines:

- **Day 0:** Matrix and cells were prepared as described in the previous section. Seeding of 40×10^3 in M231 + SMGS on 160 μL col I matrix or the Nunclon™ Delta treated surface of the 24 well multidish.
- **Day 1:** After 24 h the medium was replaced with 1 mL M231 + 1 % FBS + 5 ng/mL TGF β (or 1 mL M231 + 1% FBS).
- **Day 5:** The medium was replaced with 1 mL M231 + 1 % FBS + 10 ng/mL IL-1 β + 10 ng/mL PDGF-BB (or just 1 mL M231 + 1% FBS).
- **Day 7:** Potentially further stimulation is described in the section of the corresponding assay.

3.2 mRNA Quantification

SYBR® Green is an intercalating DNA dye that allows for the monitoring of DNA amplification. Fluorescence is measured after every amplification cycle of the PCR yielding a crossing point when signal reaches a certain threshold. A lower quantification cycle (Cq) corresponds to a higher initial DNA concentration. (Huggett and Bustin, 2011)

Quantitative PCR (qPCR) was utilized to assess the mribonucleic acid (RNA) concentration of the two reporter genes calponin 1 (CNN1) and matrix metalloproteinase 9 (MMP9) in HAoSMCs differentiated as described in section 3.1. Using the housekeeping gene glyceraldehyde-3-phosphate dehydrogenase (GAPDH) as a reference.

RNA Isolation

RNA was isolated using the Total RNA Purification Kit. The extraction was performed according to the corresponding protocol, using the extra washing step with 700 μL 80 % ethanol and eluting with 30 μL of RNase-free water.

Reverse Transcription

For RT, RNA samples were diluted to yield 10 μL of $\sim 10 \text{ ng}/\mu\text{L}$ RNA. The samples were heated for 5 min at 68°C before adding 10 μL of the RT reaction mix:

Table 3.2: Master Mix for RT

component	concentration	volume (μL)
First Strand Buffer	5x	4
DTT	???	2
dNTP	???	1
Oligos	???	1
RiboLock	???	1
M-MLVRT	???	1

The reverse transcription was carried out for 60 min at 37°C , before inactivating the enzyme for 5 min at 95°C . cDNA was used for qPCR or stored at -20°C .

qPCR

Table 3.3: Sample Composition for qPCR

component	concentration	volume (μL)
SYBR GREEN Master Mix	1:2	3.75
Primer (forward + reverse)	5 pM (each)	1.125
H ₂ O	-	1.125
cDNA	-	1.5

Samples were prepared in a 384-well Multiply PCR plate, the wells were sealed, thoroughly mixed by inversion of the plate and the assay performed with 7900HT Fast Real-Time PCR System:

Table 3.4: qPCR Cycle

step	time (s)	temperature ($^\circ\text{C}$)	loop to	passes
1	120	50		1
2	600	95		1
3	15	60		40
4	60	60	3	40
5	600	95		1
6	-	16		1

Processing of Data

The C_q was automatically calculated by the software SDS2.2.2 and exported for further analysis. The arithmetic mean of three technical replicates was calculated for each sample, disregarding values that are obvious outliers. For normalization, the mean C_q of the reference gene GAPDH was subtracted from the mean C_q of the gene of interest:

$$\Delta ct = ct(\text{gene of interest}) - ct(\text{GAPDH})$$

Taking into account the exponential amplification of DNA in PCR, the Δct can then be transformed into a relative expression level. Where 10×10^6 is just a constant to yield values that are easier to work with:

$$\text{rel.expr.} = 2^{-\Delta ct \times 10^6}$$

In total, four biological replicates were done. Data visualization and statistical analysis were done in python. Assuming a normal distribution, a student's t-test was used, and a p-value of 0.05 is considered significant. For detailed information, please refer to the script.

3.3 Energy Profiling

The Seahorse XF Analyzer allows real-time measurement of dissolved oxygen and protons in a confined small volume by using solid-state sensor probes. These are used to calculate the oxygen consumption rate (OCR) and extracellular acidification rate (ECAR) of a cell monolayer. The OCR and ECAR are indicators for mitochondrial respiration and glycolysis respectively and can be used to assess the metabolic function of cells. (Agilent Technologies, 2022)

Seahorse Assay was utilized to assess the energy profile of HAoSMCs differentiated as described in section 3.1. For this assay, cells were not differentiated in a 24 well multidish but an XF24 Cell Culture Microplates. Since the confined volume required for the assay would not fit the matrix, cells were cultivated without!

Seahorse Assay

On the day before the assay, the Seahorse XF Analyzer was turned set up to calibrate. The XF24 Extracellular Flux Assay Kit cartridge was left to equilibrate in Seahorse XF calibrant overnight at 37°C (in a non-CO₂ environment).

On the day of the assay, cells were washed with 500 μ L PBS each and afterward incubated with 500 μ L XF BASE medium, supplemented with 1 mM sodium pyruvate, 10 mM glucose, 2 mM glutamine & 90 μ M NaOH. The cells were left to incubate for 1 h at 37°C in a non-CO₂ environment. During this time toxins for disruption of the respiratory chain were prepared and loaded into the XF24 Extracellular Flux Assay cartridge:

Table 3.5: Toxin Concentrations for XF24 Extracellular Flux Assay

component	concentration in cartridge (μ M)	volume in cartridge (μ L)	concentration in well (μ M)
Oligomycin	14	55	1.4
FCCP	10	60	2.0
Antimycin	50	65	5.0

The cartridge was loaded into the XF Analyzer for calibration, after successful calibration, the hydration cartridge was replaced with the cell plate. The measurement was programmed as the following:

- Calibration of the probes.
- Equilibration
- 3 Repeats of:
 - Mixing (1 min)
 - Pause (2 min)
 - Detection of OCR and ECAR (4 min)
- Pause (2 min)
- Injection of 55 μ L Oligomycin
- 3 Repeats of:
 - Mixing (1 min)
 - Pause (2 min)
 - Detection of OCR and ECAR (4 min)
- Pause (2 min)
- Injection of 60 μ L FCCP
 - Mixing (1 min)
 - Pause (2 min)
 - Detection of OCR and ECAR (4 min)
- Pause (2 min)
- Injection of 55 μ L Antimycin
- 3 Repeats of:
 - Mixing (1 min)
 - Pause (2 min)
 - Detection of OCR and ECAR (4 min)

Finally, the medium was removed and cells were stained for 15 min with 1 μ g/mL Hoechst 33342 in PBS and photographed to determine cell count for normalization.

Processing of Data

Cells were quantified using a python script provided by Dr. Tobias Reinberger. OCR and ECAR were calculated by the XF Analyzer and normalized using the cell count and the signal in the control wells. In total, three biological repeats were recorded. One of which was excluded because no changes in OCR and ECAR could be detected and cells detached from the bottom of the wells during staining. For the remaining two replicates, the least fitting of the 5 technical repeats for each condition was manually excluded. Further, initial OCR and ECAR, as well as the characteristics of the respiratory chain displayed in figure 3.6 B, were calculated, using a modified python script provided by Dr. Tobias Reinberger. Assuming a normal distribution, a student's t-test was used, and a p-value of 0.05 is considered significant. For detailed information, please refer to the script.

3.4 Oxidative Stress Assay

CellROXTM Green is a fluorescent dye that gets oxidized in an environment of oxidative stress and then binds to DNA, showing bright-green fluorescence (Thermo Fisher Scientific

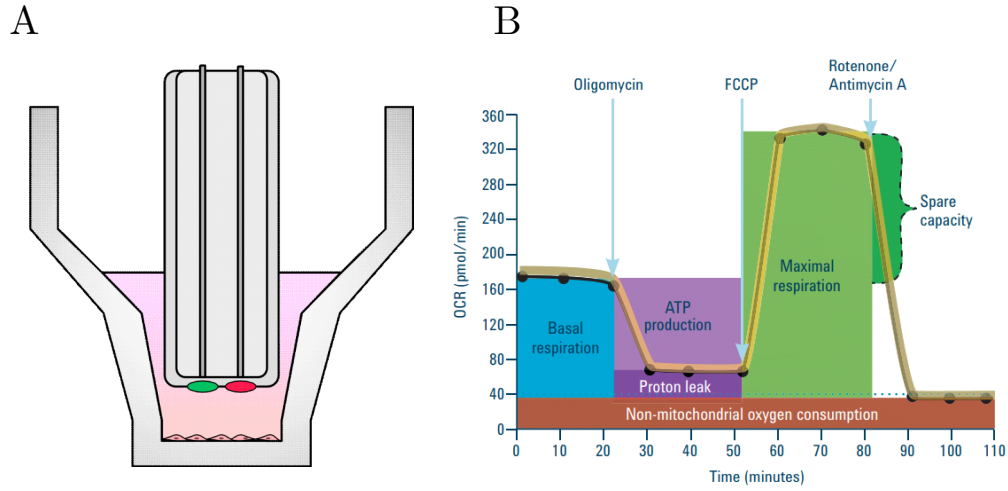


Figure 3.6: Basics of Seahorse Assay (a placeholder)

(A) Schematic of a well-used for Seahorse Assay. For the measurement, the piston in the middle lowers to the bottom, this way defining a restricted space at the bottom. OCR and ECAR in this volume are measured via two probes (red and green). (B) Exemplary curve for OCR recorded over time and extractable properties of the respiratory chain.

Inc., 2022). CellROX™ Green assay was used to assess generation of ROS in HAoSMCs differentiated as described in section 3.1. After differentiation, further stimulation (from here on referred to as *boost*) with PDGF-BB was carried out. Finally, a recovery experiment was performed using NAC, a potent antioxidant, to quench generation of ROS.

CellROX™ Assay

For the assay, cells were washed with PBS, then the boost was performed using variable concentrations of PDGF-BB in 300 μ L Hanks balanced salt solution (HBSS). For ROS quenching with NAC, 0.25 M NAC solution was added to the wells 2 h prior to the experiment and also added to HBSS during the experiment.

Table 3.7: Composition for Seahorse Assay Boost

component	concentration	final concentration	volume (μ L)
HBSS	-	-	300
PDGF	100 μ g/mL	variable (0 - 400 ng/mL)	variable
Hoechst	1 mg/mL	1 μ g/mL	0.3
CellROX™ Green (1:500)	2.5 mM	5 μ M	0.6
NAC	0.25 M	variable (0 - 8 mM)	variable
total	-	-	~300

Cells were kept at 37°C in a 5% CO₂ environment during the boost, the incubation time is indicated with the results of the respective experiment. Imaging was done with the BZ-X810 All-in-One Fluorescence Microscope, using standard sensitivity. Images for the

N-acetylcystein (NAC) quench were recorded as a z-stack and merged into one image using [KEYENCE SOFTWARE].

Processing of Data

For PDGF-BB-boost titration, 7 biological repeats were performed, of which one was excluded because of a high signal in the negative control. For NAC quench, 4 biological repeats were performed, of which one has been excluded because no signal in the positive control. For quantification of signal intensity, pixels with a green value higher than 90 were counted. Differences in cell count were adjusted by division through the number of pixels with a blue value bigger than 80. To adjust for the large variance in total signal intensity between biological repeats, values were adjusted by division through the total signal of all recorded conditions. For statistical testing, the Mann-Whitney U test was used, and a p-value of 0.05 is considered significant. For detailed information, please refer to the scripts.

3.5 Curation of Data for postGWAS Analyses

Data for postGWAS analyses and co-visualization with the GWAS data, were downloaded from public resources. Processing of the data and further annotation is briefly described in the following listing. The generated tables are summarized in figure 4.9 and table 4.8. For a complete view, please refer to the download scripts.

- **GWAS Summary Statistics:** The CAD GWAS summary statistics from Aragam et al. (2021) as well as a list of identified proxy single nucleotide polymorphisms (SNPs) from the study were annotated via the Ensembl representational state transfer (REST) application programming interface (API) by Dr. Tobias Reinberger.
- **HGNC Gene List** The newest quarterly update to the complete Human Gene Nomenclature Consortium (HGNC) dataset was downloaded via the [HGNC file transfer protocol \(FTP\) server](#). The dataset was used to generate a list of all 43135 approved symbols, mapping to their HGNC ID as well as a list of all 98723 symbols (approved, alias, and previous), mapping to their HGNC ID.
- **Linked SNPs** LD r^2 values for variants in a 500 kb window around all variants in the list of CAD GWAS proxy variants, were computed and downloaded via the [ensembl REST API](#). For humans, ensembl calculates the LD with data from the 1000 Genomes project (see table 3.8). In the same process, linked SNPs were annotated with their most severe consequence from the ensembl variant effect predictor (VEP). In total information for 449770 relationships were downloaded.

Table 3.8: 1000 Genomes Populations

Name	Size (individuals)	Description
1000GENOMES:phase3:ALL	2504	All phase 3 individuals
1000GENOMES:phase3:AMR	347	Americans
1000GENOMES:phase3:EAS	504	East Asians
1000GENOMES:phase3:EUR	503	European
1000GENOMES:phase3:SAS	489	South Asian

- **Ensembl Genome Annotation** The newest Ensembl build (Ensembl release 106) was downloaded via the [ensembl FTP server](#). Features annotated as genes of the type protein-coding (19994), lncRNA (17734), or miRNA (1877) were extracted. Further gene symbols were mapped to their HGNC ID if possible.
- **Ensembl Regulatory Build** The newest ensembl regulatory build (Ensembl release 106) was downloaded via the [ensembl FTP server](#), containing 110623 open chromatin regions, 30873 TF binding sites, 175885 CTCF binding sites, 127935 enhancers, 36597 promoters & 140548 promoter flanking regions.
- **Open Target Genetics l2g Scores** The latest list of Open Target Genetics L2G Scores was downloaded via the [open target genetics FTP server](#). Entries were annotated with their HGNC ID whenever possible, 655 entries that do not map to a gene that is approved by the HGNC were dropped, yielding a total of 3580206 database entries.
- **TSS** 35160 transcription start sites (TSS) for protein-coding genes were extracted from a [University of California Santa Cruz \(UCSC\) Genome Browser dump](#).
- **Associated traits from GWAS catalog** The SNP trait associations from the latest release of the GWAS catalog as well as the accompanying list of studies were downloaded via the [GWAS catalog FTP server](#). 14892 SNP-trait correlations missing a position on the human reference genome or the p-value for the association were dropped from the data set. Further, the column for Odds Ratio or beta was separated into two columns. In total, 370002 associations from 5831 distinct studies were collected.
- **TADs** TADs predicted by software adapted from Dixon et al. (2012) were downloaded via the [3D genome browser](#). In total, TADs in 40 distinct biosamples were downloaded.
- **scATAC-seq from Newman et al. (2021b)** Processed scATAC-seq data for 8 cell-types [SOME MORE INFO] were scraped from the [Miller Lab GitHub repository](#).
- **scATAC-seq from CATlas** Processed scATAC-seq data was scraped from the [Ren Labs website](#) for 222 biosamples.
- **ABC model** The ABC model data for 131 biosamples was downloaded from the [Engreitz Lab FTP server](#). The data was further translated from Genome Reference Consortium Human Build 37 (hg19) to Genome Reference Consortium Human Build 38 (hg38) using pyliftover.
- **ENCODE cCREs** cCREs in distinct biosamples were downloaded by Dr. Tobias Reinberger, filtering out elements that were annotated as *unclassified*.

3.6 Visualization of GWAS data

For visualization of the data, a bokeh application was built, that fetches the data from the database and renders it to a web browser (Bokeh Development Team, 2022).

Bokeh is a python module that allows easy and interactive visualization of data. It combines the powerful data processing tools of python with the interactivity of javascript (JS) running in the browser. The python side of bokeh creates python objects which are serialized into JavaScript Object Notation (JSON) data and handed over to bokehJS which deserializes them into JS objects that are rendered to the browser. The integrated bokeh server additionally offers the possibility to synchronize data between the underlying python environment and browser-side JS library, allowing real-time updates to the displayed data.

According to good design principles, the concerns of the application are split into two sections, as shown in fig. 3.9. Reading of data from the database and further processing

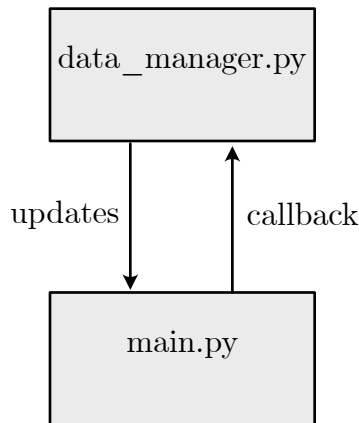


Figure 3.9: Architecture of the GWAS Navigator

steps are managed by a data provider and enclosed in one class. In contrast to the model-controller-view architecture, a popular architectural pattern for the design of user interfaces, there is no partition between a view and a controller (Langtangen and Johansen, 2015). Since data visualization, as well as the control widgets, are created by bokeh, it is convenient to use the built-in event listeners of the library to handle the required callbacks. Therefore, the main file is responsible for the creation of all plots and widgets as well as listening for inputs.

3.7 Enrichment analysis

Based on the data in the database, initial postGWAS studies were run. Annotation enrichment analyses are a popular tool for the identification of terms that are over-represented in a list of interest. The most prominent application is their application as gene set enrichment analysis (GESA). GESAs are used to check for the overrepresentation of a candidate gene list in a predefined set of genes (Tipney and Hunter, 2010). In this case, the method is used to determine if cCREs overlaps with CAD associated SNPs is enriched in certain biosamples, using Fisher’s exact test.

For the analysis, cCREs annotated as unclassified were excluded. As a list of CAD associated SNPs the list of 241 proxy variants from the database was used, as well as all linked variants ($r^2 \geq 0.6$) in the 1000 Genomes European Population. The following parameters were calculated for all biosamples:

- The number of distinct cCREs among all biosamples (m)
- The number of distinct cCREs that are annotated in the biosample of interest (mt)
- The Number of distinct cCREs that overlap with an SNP in the SNP list in any biosample (n)
- The Number of distinct cCREs that overlap with an SNP in the SNP list in the biosample of interest (nt)

The p-value for the number of overlaps to be greater than or equal to the observation can be calculated as the cumulative distribution function of the hypergeometric distribution.

3 Methods

$$P(\sigma_t \geq n_t) = \sum_{k=n_t}^{\min(m_t, n)} \frac{\binom{n}{k} \binom{m-n}{m_t-k}}{\binom{m}{m_t}}$$

To account for the multiple comparisons problem, p-values were adjusted with Bonferroni correction where n is the number of tests (\equiv number of biosamples):

$$p_{adj.} = p * n$$

The analysis and visualization were done in python. An adjusted p-value of 0.05 is considered significant. Finally, the identified biosamples were annotated via the [cell line database Cellosaurus](#). For detailed information, please refer to the analysis scripts.

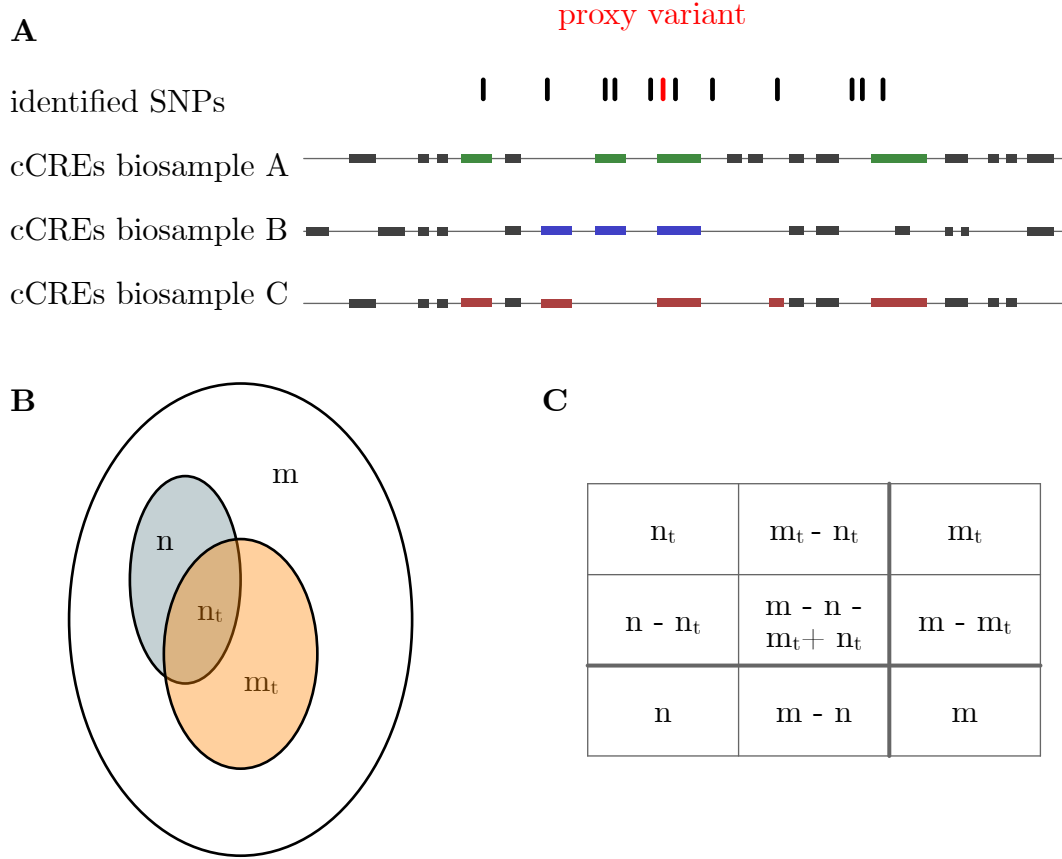


Figure 3.10: Enrichment analysis for cCREs overlapping with CAD risk SNPs

(A) Visual representation of the overlap calculation for enrichment calculation. The proxy variant is indicated as a red line, variants in LD are indicated as black lines. cCRE are shown as boxes, those that are overlapping with an SNP were colored according to the biosample they were annotated in. (B) Venn diagram of these values for a biosample. (C) Schematic contingency table for a biosample. (m) is the number of distinct cCREs found among all biosamples (23 in this example); (m_t) the number of distinct cCREs annotated in the biosample of interest (16 for biosample A, 14 for biosample b, 14 for biosample C); (n) the number of distinct cCREs overlapping with an SNP (6 in this example); the number of distinct cCREs overlapping with an SNP in the biosample of interest (4 for biosample A (green), 3 for biosample B (blue), 5 for biosample C (red))

4

Results

4.1 Differentiation

To characterize the influence of PDGF-BB stimulation on HAoSMCs, the cells were first treated with TGF β for 2 d to push them towards a phenotype that resembles the contractile phenotype. From this standardized starting point, cells were stimulated for 4 d with IL-1 β and PDGF-BB. The induced phenotypes were then characterized via qPCR and Seahorse Assay.

Expression of CNN1 & MMP9

To confirm that the HAoSMCs first adopt a contractile phenotype and to track further differentiation after stimulation with PDGF-BB, the mRNA levels of the marker genes CNN1 as well as MMP9 were determined using qPCR. CNN1 as a contractile marker and MMP9 as a marker for a synthetic phenotype. For better comparability, mRNA levels are considered in relation to the housekeeping gene GAPDH.

As seen in figure 4.1 (top panel), stimulation of HAoSMCs cultivated on a col I-matrix with TGF β causes a significant increase in CNN1 expression (+– vs. – –). After further stimulation with PDGF-BB & IL-1 β , while not significant, CNN1 expression declines again (+– vs. ++) but is still significantly higher than in HAoSMCs which were not stimulated (– – vs. ++). A similar trend is noticeable for HAoSMCs cultivated on plastic, even when not significant after four biological repeats. Additionally, stimulation of HAoSMCs on plastic with TGF β followed by stimulation with PDGF-BB & IL-1 β , yields a significantly higher expression of CNN1 (++ Matrix vs. ++ Plastic).

As seen in the bottom panel of figure 4.1, after 4 biological repeats, no statistically significant trends can be observed for the expression of MMP9. Still the average expression of MMP9 seems to be doubled for all conditions, the most prominent difference being between HAoSMCs treated first with TGF β as well as with PDGF-BB & IL-1 β (++ Matrix vs. ++ Plastic, $p = 0.063$).

Energy profile

In addition to the expression of CNN1 & MMP9, the energy profiles of HAoSMCs were assessed via Seahorse Assay. It is important to note, that the assay was carried out on

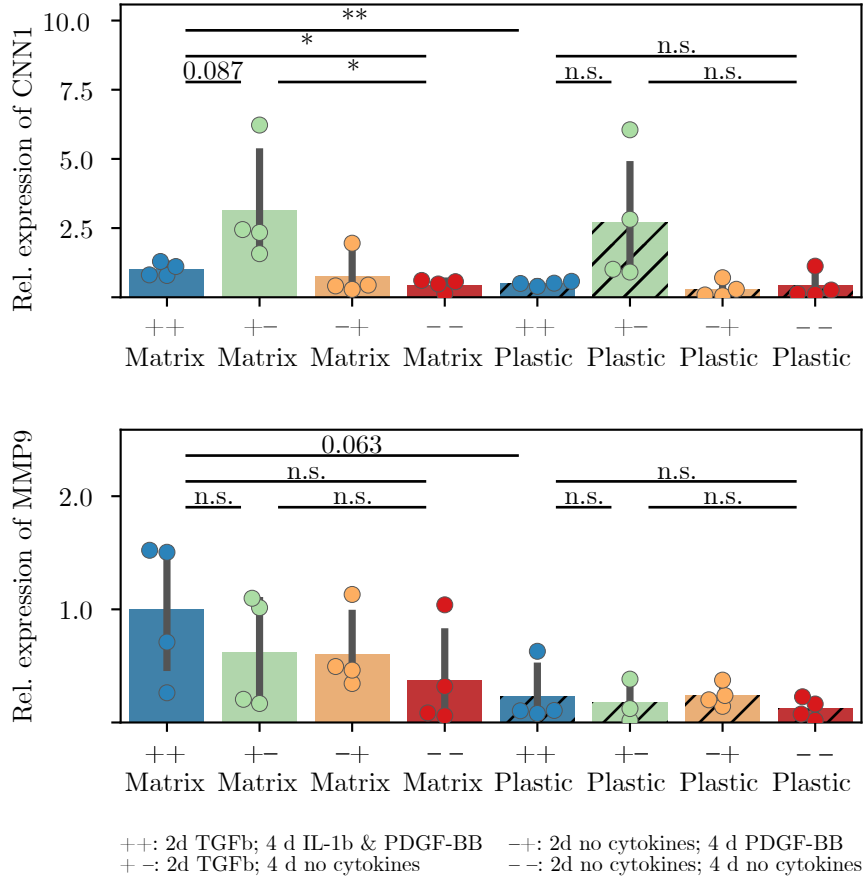


Figure 4.1: Relative Expression of CNN1 & MMP9 in HAoSMCs

qPCR analysis of expression for contractile marker CNN1 (top) and synthetic marker MMP9 (bottom) for HAoSMCs differentiated with different combinations of cytokines: ++: 2 d with TGF β followed by 4 d with IL-1 β & PDGF-BB; +-: 2 d with TGF β followed by 4 d without stimulation; -+: 2 d without stimulation followed by 4 d with IL-1 β & PDGF-BB; --: 6 d without stimulation. All four conditions were tested on two different surfaces (plastic vs. col I matrix). Expression levels are in relation to expression of housekeeping gene GAPDH. Statistical analysis for (n = 4) biological repeats was performed using student's T-test: * : $p < 0.05$; ** : $p < 0.01$

plastic because the col I matrix does not fit into the confined compartment created by the piston for detection of OCR & ECAR. Further, only two biological repeats were evaluated, because it became increasingly clear, that all other experiments would be carried out on a col I matrix. Therefore all the following results should be considered under these circumstances.

The readout parameters of the Seahorse assay are the OCR as a representation of mitochondrial activity and the ECAR, representing the glycolytic activity of the cells. OCR and ECAR for HAoSMCs are displayed in figure 4.2. All cells show characteristic changes in OCR after addition of toxins impacting the respiratory chain (compare to figure 3.6 B). After inhibition of the ATP synthase with Oligomycin, the basal OCR drops, this way making

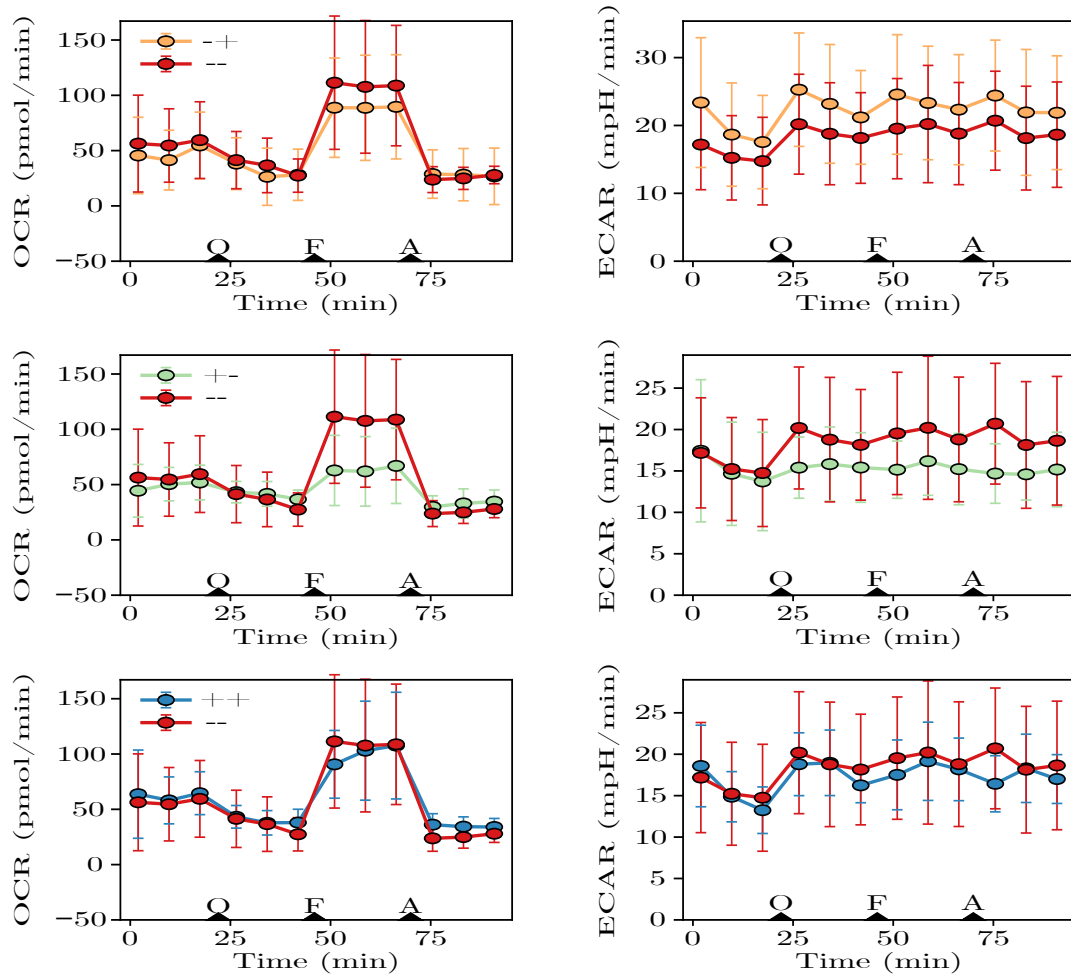


Figure 4.2: OCR & ECAR of HAoSMCs

Seahorse assay for HAoSMCs differentiated with different combinations of cytokines. ++: 2d with TGF β followed by 4d with IL-1 β & PDGF-BB; +-: 2d with TGF β followed by 4d without stimulation; -+: 2d without stimulation followed by 4d with IL-1 β & PDGF-BB; —: 6d without stimulation. OCR & ECAR are shown for +- (top), +- (middle) and ++ (bottom) in comparison to —. Injection times for toxins (O: Oligomycin; F: FCCP; A: Antimycin A) are marked as triangles. All tracks were recorded for cells cultivated on plastic. Shown data-points are the average of (n = 2) biological repeats.

the proportion of the OCR accessible that was required for adenosine triphosphate (ATP) production. Further, the addition of FCCP decouples the respiratory chain, destroying the proton gradient over the mitochondrial membrane and letting the cells reach their maximal respiratory capacity. Finally, the inhibition of coenzyme Q-cytochrome c reductase (complex III) with Antimycin A, stops all mitochondrial respiratory activity.

The ECAR shows a mild increase for all conditions after the addition of Oligomycin, most likely because the cells are compensating for the loss of mitochondrial ATP production via increased glycolysis.

4 Results

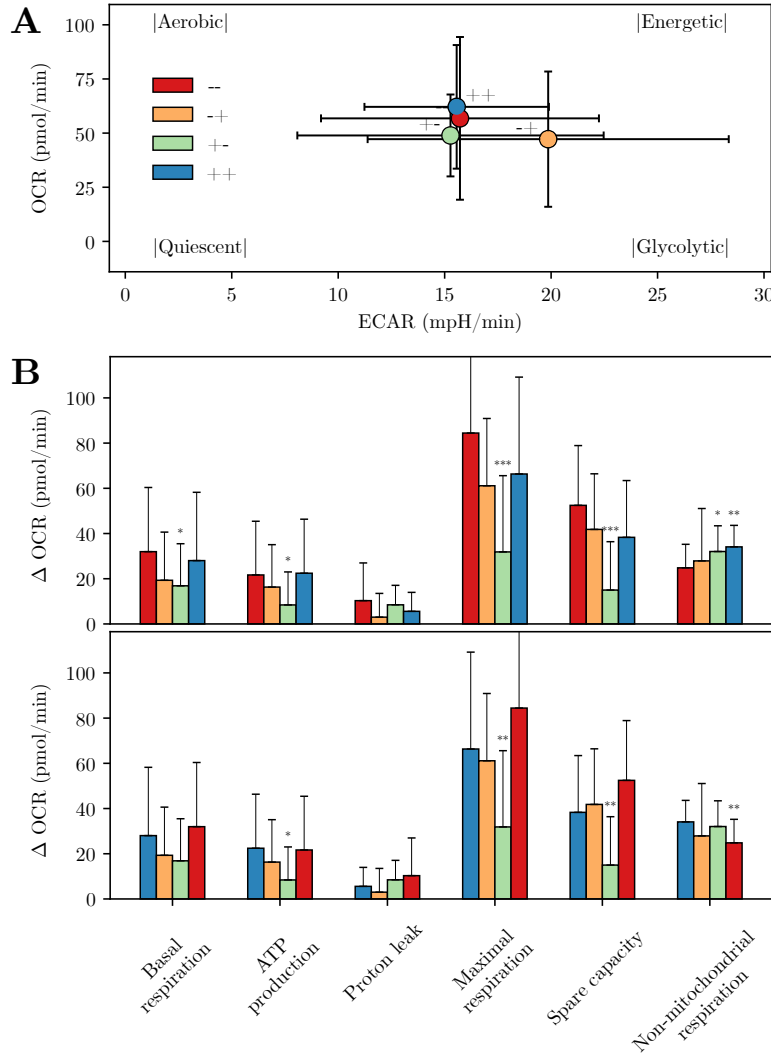


Figure 4.3: Energy profile of HAoSMCs

Seahorse assay for HAoSMCs differentiated with different combinations of cytokines as described in figure 4.2. (A) Initial OCR & ECAR of the four tested conditions. (B) Characteristics of the respiratory chain calculated from the tracks shown in figure 4.2 as described in section 3.3. Statistical analysis for ($n=2$) biological repeats was performed using student's T-test: * : $p < 0.05$; ** : $p < 0.01$; *** : $p < 0.001$

Looking at the energy profile of the HAoSMCs it is easy to see that OCR & ECAR are quite similar for the conditions ++, +- and -. The only outlier showing a higher ECAR, are HAoSMCs only stimulated with only IL-1 β & PDGF-BB (-+) (fig. 4.3, A). More interesting differences can be observed when examining characteristics of the respiratory chain. Stimulation with only TGF β causes a significant decrease in basal respiration, ATP production, maximal respiration as well as spare capacity (figure 4.3, B top). Further stimulation with IL-1 β & PDGF-BB then causes a significant increase of these parameters to similar levels as in initially dedifferentiated HAoSMCs (figure 4.3, B bottom).

4.2 Evaluation of oxidative Stress

Finally, it was evaluated if further stimulation with PDGF-BB would yield the generation of ROS to an extent that can not be compensated by the ROS defense and lead to oxidative stress.

PDGF boost of out cells induces oxidative stress

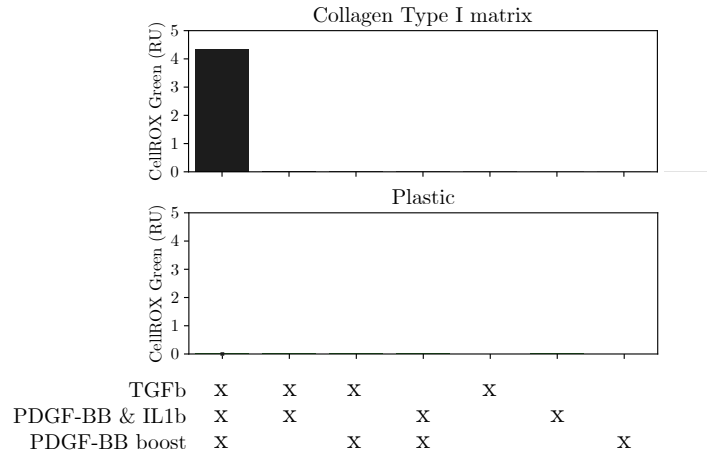


Figure 4.4: Boost with PDGF-BB induces generation of ROS.

CellROX™ assay for HAoSMCs differentiated with different combinations of cytokines: 2 d with TGFβ; followed by 4 d with IL-1β & PDGF-BB; followed by 2 h boost with 200 ng/mL PDGF-BB. Differentiation and assay carried out on col I matrix (top) or plastic (bottom). The hown signal was calculated according to section 3.4 as the CellROX™ Green signal, normalized by Hoechst 33342 signal. No statistical analysis for (n = 1) biological repeats was performed.

At first, an experiment already done in the group was repeated. Stimulating the four tested combinations for 2 additional hours with 200 ng/mL PDGF-BB in HBSS. As displayed in figure 4.4 only stimulation for 2 d with TGFβ, followed by 4 d with IL-1β & PDGF-BB, followed by a 2 h boost with PDGF-BB, was able to trigger noticeable generation of ROS for cells cultivated on col I-matrix. No generation of ROS was detectable for HAoSMCs cultivated without the col I-matrix.

Characterization of the CellROX™ Assay

To get a better understanding of the assay and its limits, a titration was carried out. For this, HAoSMCs stimulated for 2 d with 5 ng/mL TGFβ as well as 4 d with 10 ng/mL IL-1β & 10 ng/mL PDGF-BB, were boosted with different concentrations of PDGF-BB (0 - 400 ng/mL). Signal was detected after 60, 120, 180 & 240 min in HBSS. As seen in figure 4.5, CellROX™ Green signal is negligible after 60 min and then increases with elongated boost times. Further, CellROX™ Green signal stays negligible for boost concentrations < 100 ng/mL PDGF-BB. After 180 and 240 min (figure 4.5 B top & middle), CellROX™ Green signal is significantly increased for boost with 200 ng/mL PDGF-BB in comparison to no

4 Results

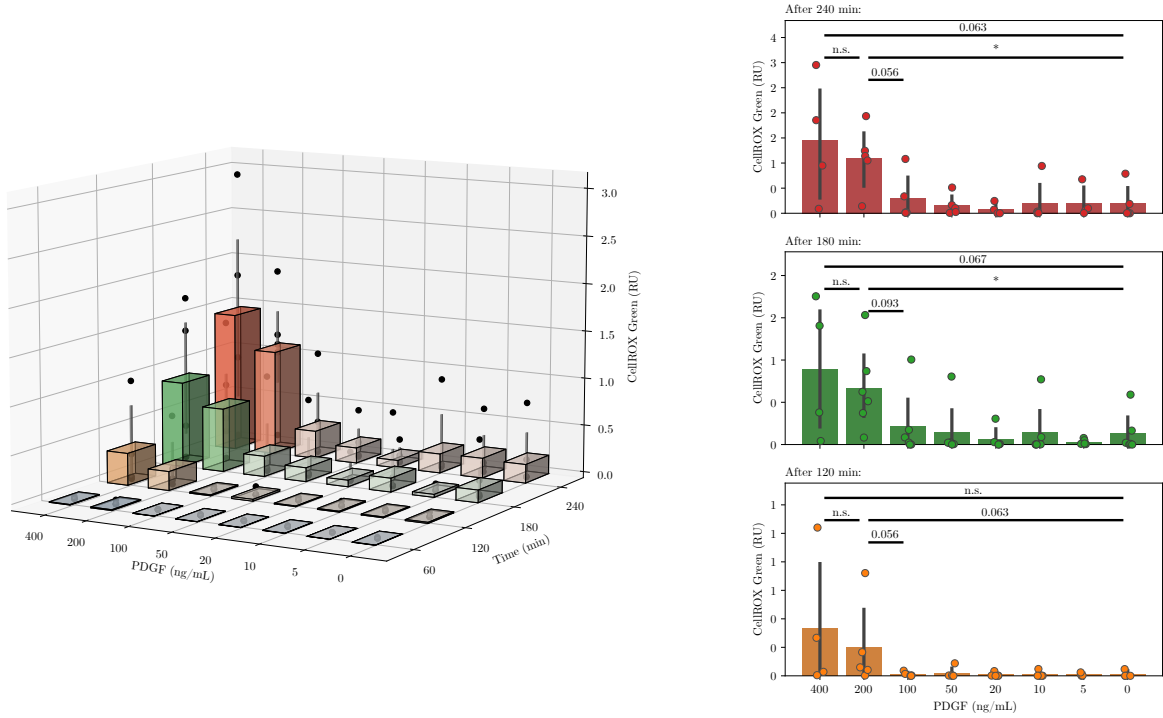


Figure 4.5: PDGF-BB boost titration

CellROX™ assay for HAoSMCs differentiated with different combinations of cytokines: 2 d with TGF β ; followed by 4 d with IL-1 β & PDGF-BB; followed by 4 h boost with 0-400 ng/mL PDGF-BB. Differentiation and assay carried out on col I matrix. (A) 3D visualization: CellROX™ Green signal as a function of PDGF-BB concentration during the boost as well as incubation time. (B) 2D visualization: CellROX™ Green signal as a function of PDGF-BB concentration after 120 min, 180 min & 240 min. The shown signal was calculated according to section 3.4 as the CellROX™ Green signal, normalized by Hoechst 33342 signal. Statistical analysis for ($n=6$) biological repeats was performed using Mann-Whitney U test: * : $p < 0.05$; ** : $p < 0.01$. It is important to note that not for every biological repeat, *all* PDGF-BB concentration were tested.

boost. While the signal in wells boosted with 400 ng/mL PDGF-BB was on average higher than the signal after boost with 200 ng/mL PDGF-BB, this increase was not reproducible. In two repeats the signal was extremely high, in the other two repeats it collapsed.

Overall, the trend of greatly increased CellROX™ signal for boost with 100 as well as 200 ng/mL PDGF-BB was consistent within biological repeats, however variance between repeats was almost as high as differences between the conditions. Potential causes for this phenomenon are discussed in section ???. To account for this large variation between biological repeats, the assay was reevaluated by the selection of shared conditions among the biological repeats, that were normalized by the cumulative intensity of all conditions of the biological repeat (see figure 4.6). This way compensating for differences between biological repeats. The observations stays the same: CellROX™ Green signal after 180 and 240 min is significantly higher for cells boosted with 200 ng/mL PDGF-BB than cells that

4 Results

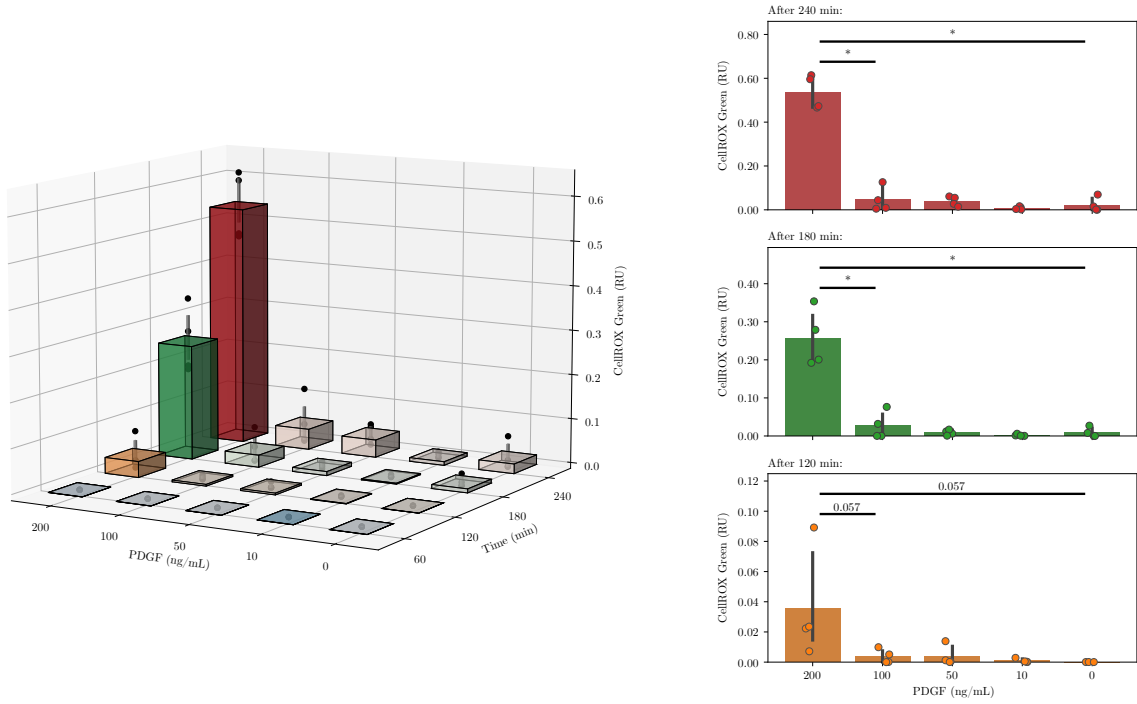


Figure 4.6: PDGF-BB boost titration - normalized

CellROX™ assay for HAoSMCs differentiated with different combinations of cytokines: 2 d with TGF β ; followed by 4 d with IL-1 β & PDGF-BB; followed by 4 h boost with 0-200 ng/mL PDGF-BB. Differentiation and assay carried out on col I matrix. (A) 3D visualization: CellROX™ green signal as a function of PDGF-BB concentration during the boost as well as incubation time. (B) 2D visualization: CellROX™ green signal as a function of PDGF-BB concentration after 120 min, 180 min & 240 min. Shown signal was calculated according to section 3.4 as the CellROX™ Green signal, normalized by Hoechst 33342 signal, further the signal was normalized via the total signal of the biological repeat. Statistical analysis for (n=4) biological repeats was performed using Mann-Whitney U test: * : $p < 0.05$; ** : $p < 0.01$.

were not boosted (0 ng/mL PDGF-BB).

Rescue of ROS production using NAC

Finally, a rescue experiment was performed, to verify that the observed signal in the CellROX™ assay was indeed due to the generation of ROS. For this, ROS generation was quenched by the addition of 2, 4, or 8 mM of NAC. Indeed, while not statistically significant after 3 repeats, a clear trend can be observed: HAoSMCs treated with NAC show no signal.

In the end, it should be noted, that the signal only builds up over 15-20 min under the microscope after the cells were taken out of the incubator. This indicates that generation of ROS might not be exclusively triggered by PDGF-BB boost but could also require additional contributors like the loss of the optimized atmosphere of 37°C and 5% CO₂ in the

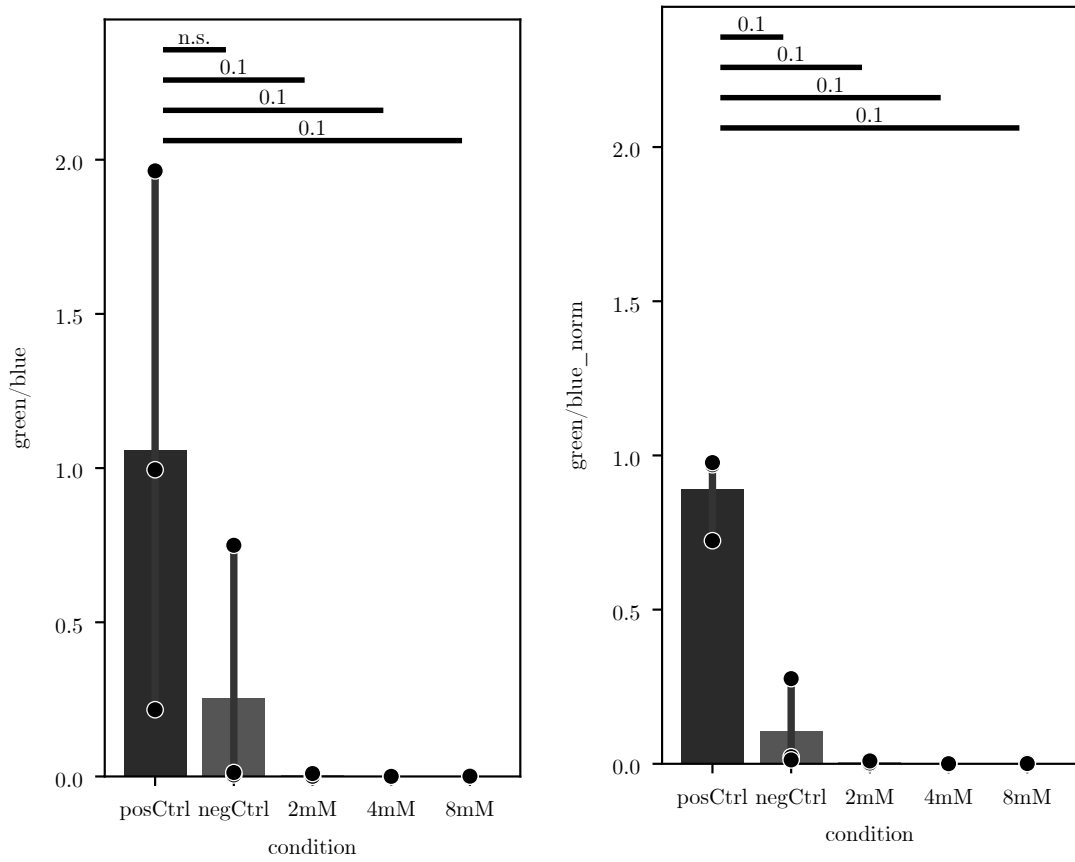


Figure 4.7: ROS generation due to PDGF-BB boost can be rescued with NAC

CellROX™ assay for HAoSMCs differentiated with different combinations of cytokines: 2 d with TGF β ; followed by 4 d with IL-1 β & PDGF-BB; followed by 3 h boost with 200 ng/mL PDGF-BB. Differentiation and assay carried out on col I matrix. Cells were treated with 2, 4, or 8 mM of NAC 2 h before the assay. Shown signal was calculated according to section 3.4 as the CellROX™ Green signal, normalized by Hoechst 33342 signal (A), further the signal was normalized via the total signal of the biological repeat (B). Statistical analysis for (n=4) biological repeats was performed using Mann-Whitney U test: * : $p < 0.05$; ** : $p < 0.01$. pos Ctrl: not treated with NAC, negCtrl: no boost with PDGF-BB

incubator. This might not have been noted during the titration assay, because cells were taken out of the incubator after one hour to image them for the first time.

4.3 Database and GWAS Visualizer

Curation of Data

Table 4.8: List of Database Tables

List of all the datasets and corresponding tables which were funneled into the database. For primary keys, foreign keys as well as fields on which an index exists, please consult figure 4.9. The size of the tables (and accompanying indices) is indicated by the number of databank pages that are reserved for the data, each page fitting 4096 bytes.

Data	Tables	Page count (including indices)
GWAS Summary stats	variation	418318
	gwas_meta_cad	867025
	identified_proxy_SNPs_tbl	4
HGNC gene list	hgnc_all_symbols_tbl	826
	hgnc_approved_symbols_tbl	592
Linked SNPs	linked_SNPs_tbl	8819
	population_tbl	1
	consequence_tbl	1
Ensembl Genome Annotation	ensembl_genelist_tbl	613
	ensembl_genelist_biotypes_tbl	1
Ensembl Regulatory Build	ensembl_reg_build_tbl	8778
	ensembl_reg_build_features_tbl	1
TSS	tss_tbl	481
Open Target Genetics Scores	opentarget_l2g_tbl	40984
GWAS catalog	gwascatalog_associations_tbl	10569
	gwascatalog_studies_tbl	326
TADs	tad_tbl	902
	tad_sample_tbl	1
scATAC seq textcite{}	clint_miller_tbl	12370
	clint_miller_biotypes_tbl	1
scATAC seq CATlas	catlas_tbl	308574
	catlas_biotypes_tbl	3
ABC model	abc_tbl	153920
	abc_targetgenes_tbl	84
	abc_celltypes_tbl	3
	abc_classes_tbl	1
ENCODE cCREs	ENCODE_CCRC	4451476
	ENCODE_CCRC_META	107
total	-	6284781 (\approx 25.75 GB)

The first step towards visualization of GWAS data and GWAS studies, was the curation of suitable complementary data. Datasets from a diverse set of data sources were downloaded and funneled into an SQLite3 database according to section 3.5. A structured query language (SQL) database is a two-dimensional relational database that allows easy and fast access to the data for visualization purposes. The types of data and their applications are briefly described in section 1.6. All database tables as well as their sizes are

4 Results

summarized in table 4.8. The relationships between the tables as well as fields serving as a primary key, foreign or fields on which an index exists, are summarised in the databases entity-relationship (ER) diagram in figure 4.9.

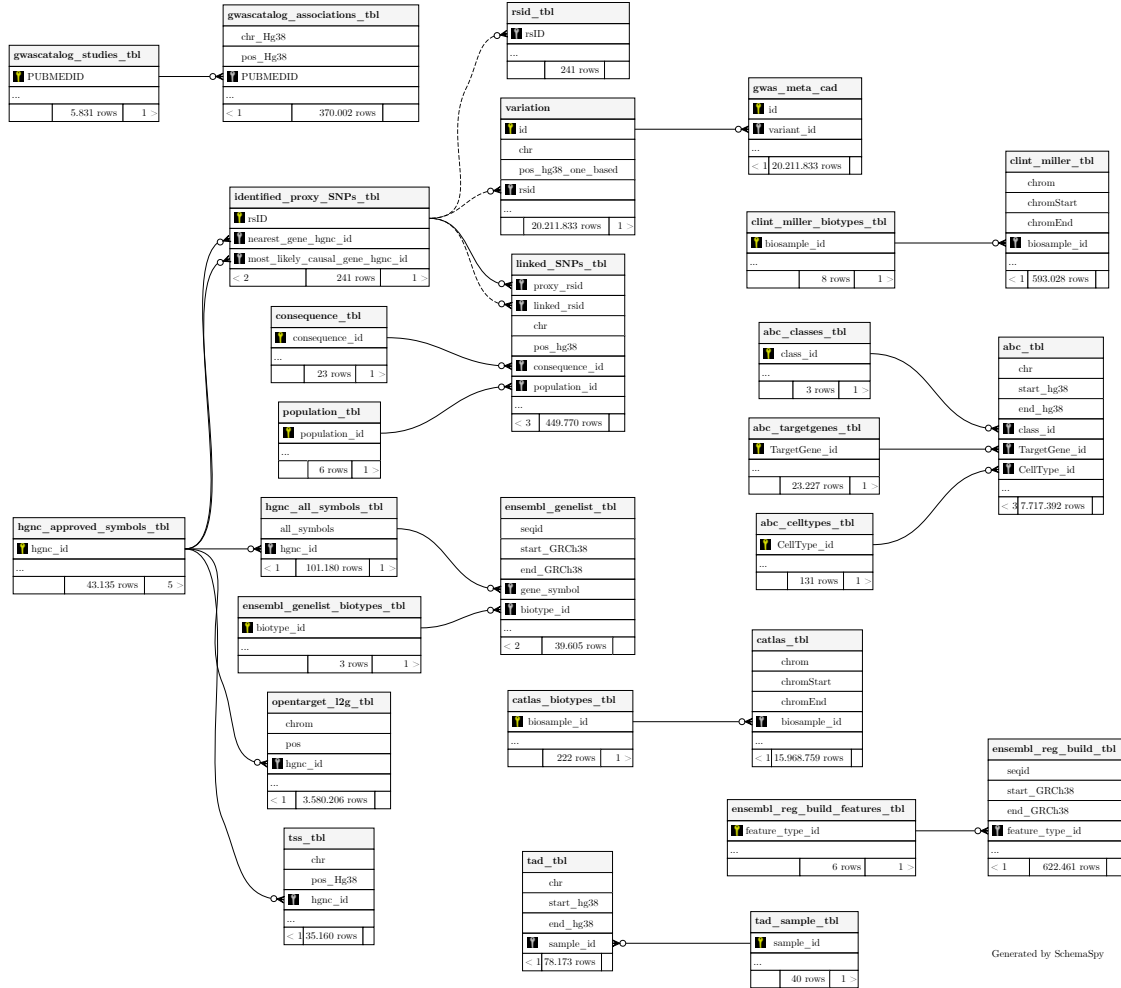


Figure 4.9: Entity-Relationship Diagram of the Database

Fields and relationships of the tables listed in table 4.8. Primary keys are marked with a golden key icon, fields serving as an foreign key are marked with an gray key icon. On fields which names are spelled out but which do not have an key icon and index exists. The diagram was generated via SchemaSpy.

A tool to visualize GWAS summary statistics for intuitive exploration.

GWAS data for coronary artery disease. Annotated with associated phenotypes from GWAS catalog, genomic features from ensembl.org, aligned with scATAC-seq data from CATlas as well as promotor enhancer interactions in form of ABC scores.

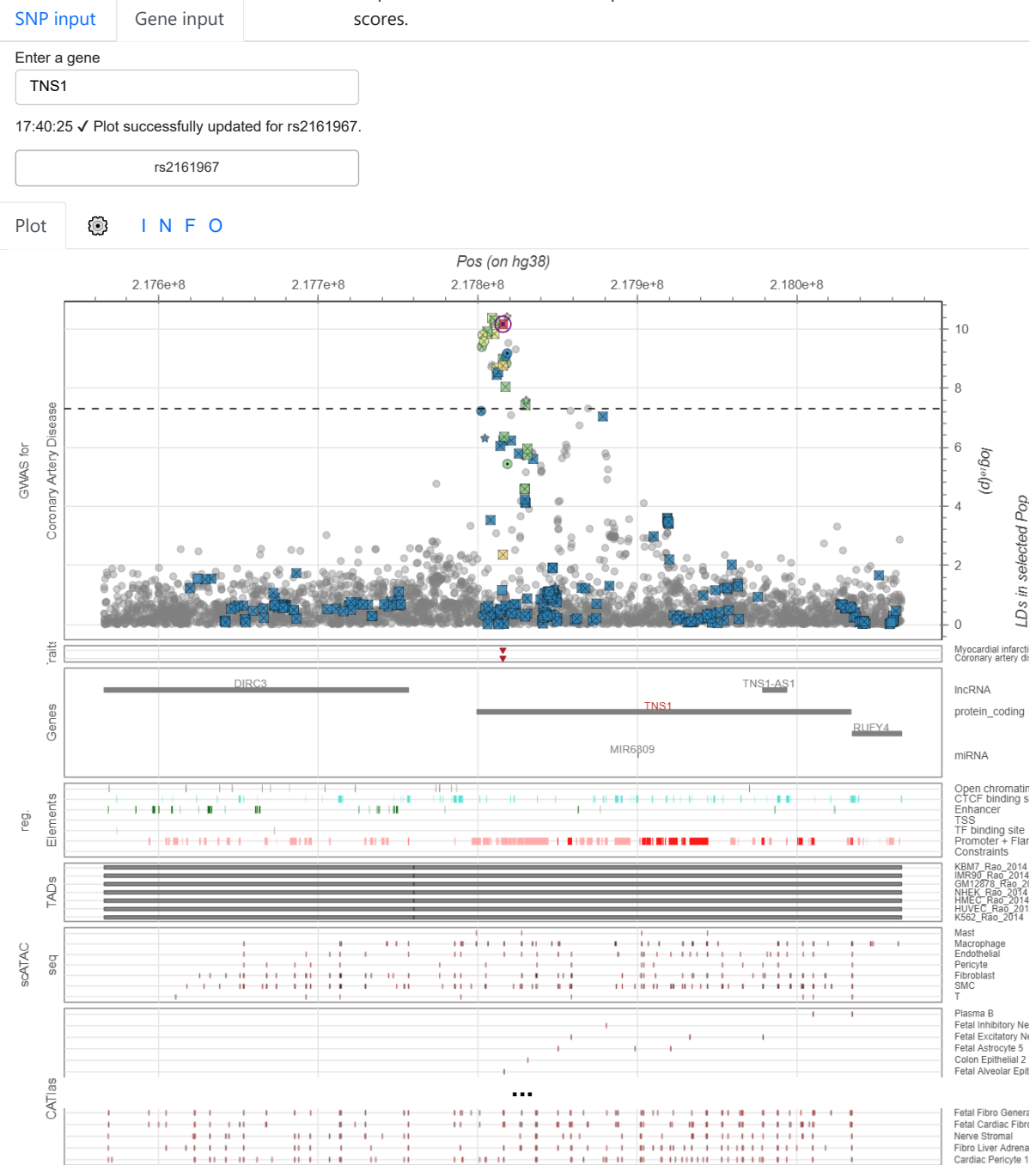


Figure 4.10: The GWAS Navigator

General content of the GWAS Navigator. The tool contains a manhattan plot with GWAS summary statistics, containing an additional annotation for variants that are in LD with the variant central to the analysis. Further variants identified as proxy variants for other phenotypes are included. Finally, the data is aligned with genomic elements such as genes, regulatory elements, scATAC-seq data as well as the ABC model. More details can be assessed by a hover effect as shown in figure 4.11.

Visualization

Implementing the initially intended use case for the data, a visualization tool for GWAS summary statistics was built according to section 3.6. As shown in figure 4.10, the GWAS Navigator consists of a split search bar which has a field to specifically search for variants by their rsID as well as a field that allows searching for genes by their symbol. In case the searched gene is associated with one of the proxy variants in Aragam et al. (2021), the tool returns a list of these variants, else the tool returns the most significant variant in the proximity of the searched gene. After a variant was chosen, the tool displays the GWAS summary statistics in a 500 kb window centered around the selected variant, to the output panel. GWAS summary statistics are visualized as a zoomed-in Manhattan plot, showing the position of a variant on hg38 on the x-axis and its p-value on the y-axis. r^2 values of variants in LD are color-coded, the most severe consequence for all linked variants predicted by VEP is indicated by the type of glyph. The minor allele frequency (MAF) and effect size (β) are included in the hover overlay (figure 4.11 A). Below this plot, variant trait associations from the GWAS catalog are indicated for variants that are in LD with the variant central to the analysis (figure 4.11 B). Further, the region is aligned with protein-coding genes, lncRNAs & miRNAs as annotated in Ensembl, and the names of genes that are associated with the variant central to analysis (open target genetics L2G score > [FIND THE THRESHHOLD]) are labeled in red. In addition, regulatory elements from the Ensembl regulatory build are displayed. Finally, scATAC-seq data and enhancers-promotor links from the ABC model were aligned, automatically hiding tracks that have no elements in the visualized region. The GWAS visualizer additionally has a settings tab, in which individual tracks can be hidden.

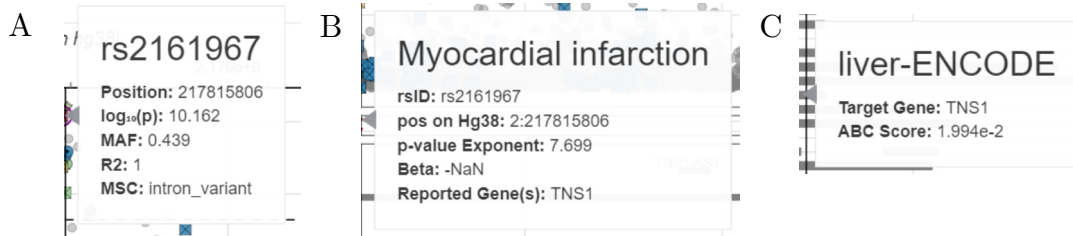


Figure 4.11: The GWAS Visualizer - Hover effect

Exampalry hover effects for features displayed in the GWAS Navigator. (A) Hover for variants in the manhattan plot. (B) Hover for variant phenotype associations. (C) Hover for cell type specific enhancers in the ABC model.

4.4 Enrichment analysis

The only data that is not displayed in the plot are ENCODE cCREs which were used for an enrichment analysis. Checking the annotated biosamples for significant enrichment of cCREs that are overlapping with proxy SNPs identified in the CAD GWAS or variants that are in LD with these ($r^2 > 0.6$). For more details please refer to section 3.7.

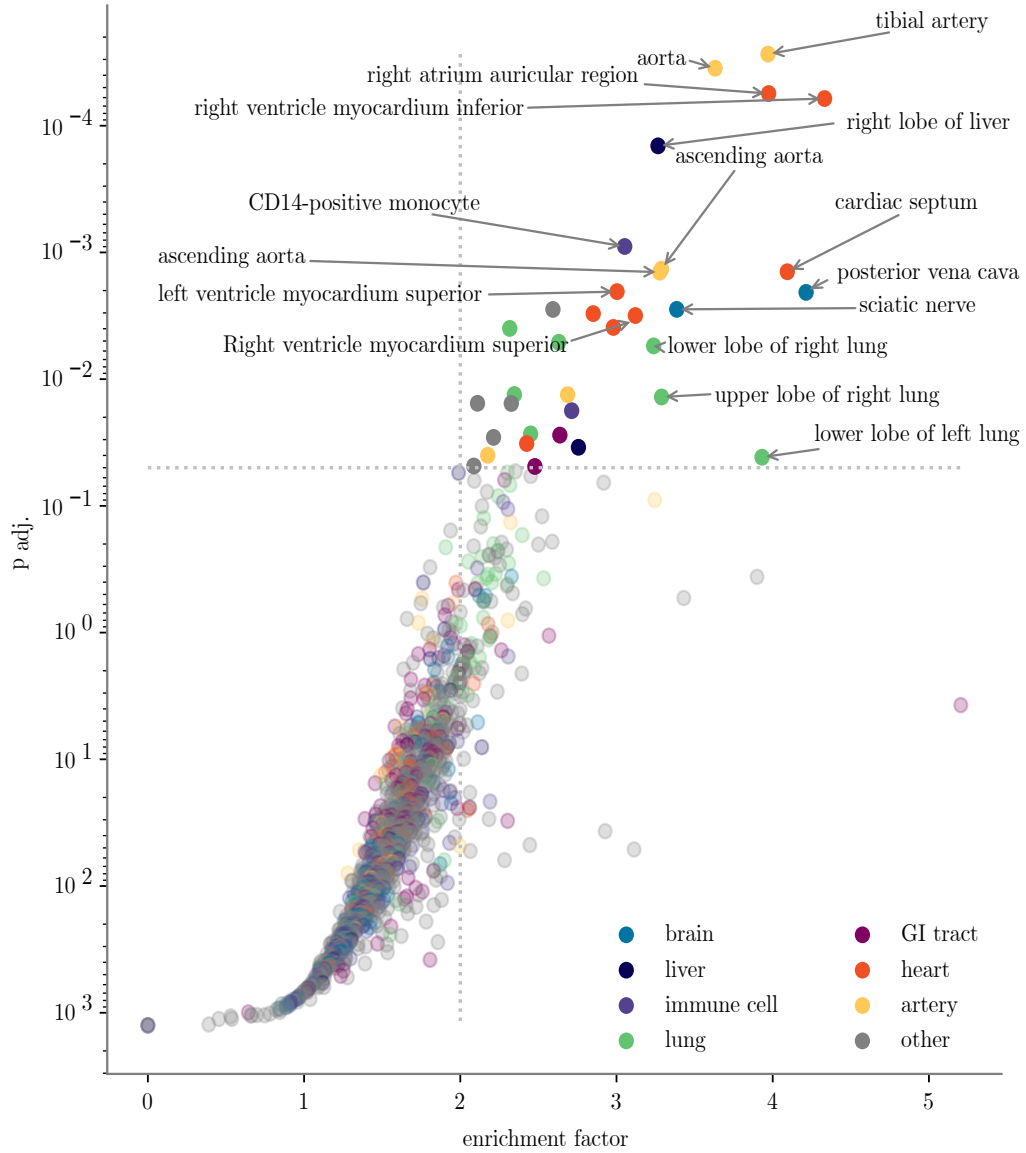


Figure 4.12: Enrichment Analysis for overlap of CAD GWAS proxy variants with tissue specific cCREs

p-values and enrichment factors for the overlap of CAD GWAS proxy variants (and variants in LD) and tissue specific cCREs. For details please refer to section 3.7.

As seen in figure 3.10, statistical significant enrichment ($p_{adj.} < 0.05$) was observed for 34 biosamples. Using the biosample annotations from Cellosaurus, these biosamples were assigned to their tissue of origin. As summarized in table 4.13 most prominent groups of origin tissues were the heart (8), the lungs (7), and arteries (6). Followed by the liver, the gastrointestinal (GI) tract, the brain, and immune cells (CD+ monocytes).

Table 4.13: Tissues Found in the Enrichment Analysis

Tissues of biosamples which show statistically significant overlap between CAD GWAS proxy variants (and variants in LD) and cCREs.

tissue	count in significant biosamples
heart	8
lung	7
artery	6
liver	2
GI tract	2
brain	2
immune cell	2
other	5
total	34

5

Discussion

5.1 PDGF-BB Signaling Seems to Induce a Synthetic Phenotype in HAoSMCs

The crucial role of VSMCs in atherogenesis has been the subject of intense research for the last few decades (Grootaert and Bennett, 2021; Yap et al., 2021). While it has traditionally been assumed that they adopt a protective role by stabilizing the arteriogenic plaque. This model is rapidly evolving and starting to consider the existence of a diverse set of dedifferentiated phenotypes (Liu and Gomez, 2019). A central hub of this process is an initial dedifferentiated mesenchymal-like phenotype, that displays the reduced expression of contractile markers and a proliferative phenotype (Yap et al., 2021). It is thought to be initiated by the TF KLF4, which induces expression of mesenchymal markers such as stem cell antigen-1 (Sca1) (Yap et al., 2021). Amongst other pathways, KLF4 expression can be induced by PDGF-BB signaling (Liu et al., 2005) specificity protein 1 (Sp1) (Deaton et al., 2009). Additionally, PDGF-BB suppresses the contractile phenotype by phosphorylation of ETS like-1 protein (Elk-1) (Wang et al., 2004) as well as the expression of dedicator of cytokinesis 2 (Dock2) (Guo et al., 2015), both of which disrupt myocardin/serum response factor (SRF) mediated expression of contractile genes. The mesenchymal-like phenotype is postulated to serve as a precursor for other dedifferentiated VSMCs phenotypes (Yap et al., 2021).

The contractile expression profile of differentiated VSMCs is constantly maintained by myocardin/SRF signaling (Long et al., 2008) and external stimulation by the extracellular matrix (ECM) and cytokines such as $TGF\beta$ (Davis-Dusenbery et al., 2011). HAoSMCs used in this thesis, seem to have initially adopted a dedifferentiated phenotype, characterized by the loss of contractile marker CNN1 (Owens et al., 2004) (figure 4.1 top). When stimulated for two days with $TGF\beta$, HAoSMCs display increased expression of CNN1. Additionally, this phenotype shows a significant decrease in basal mitochondrial respiration, ATP production and maximal respiration (figure 4.3 B top), possibly adapting to the energetic needs of the contractile phenotype, which is considered to be quiescent (Dobnikar et al., 2018). Further stimulation for 4 additional days with PDGF-BB & IL-1 β , yields a (not quite significant after four biological repeats, $p = 0.087$) drop in CNN1 expression (figure 4.1) as well as a rebound of basal mitochondrial respiration, ATP production as well as maximal respiration to similar levels as for initially dedifferentiated VSMCs (figure 4.3

B bottom).

Another important aspect of phenotypic transition and plaque development is the remodeling of the ECM by matrix metalloproteinases (MMPs) (Johnson, 2017). While not significant in 4 biological repeats, PDGF-BB-induced dedifferentiation seems to increase the expression of MMP9 for HAoSMCs cultivated on col I matrix (figure 4.1 bottom). MMP9 is an important component of atherosclerogenesis (Galis et al., 1994) and a biomarker for advanced atherosclerotic lesions (Langley et al., 2017). The fact that this trend is only observable for cells cultivated on col I (figure 4.1 bottom, $p = 0.063$), underlines the bi-directionality of the ECM-VSMC-interactions and the complexity of VSMC dedifferentiation.

Of course the acpdgf-induced phenotype can not be grasped with only two markers and requires a more indepth analysis.

5.2 CellROX™ Green is Suitable for Assessing ROS Generation in HAoSMCs

Evaluating the response to further stimulation with PDGF-BB, the CellROX™ Assay was able to confirm a result previously observed in the group (unpublished). Stimulation of HAoSMCs cultivated on col I matrix and stimulated for 2 days with TGF β and 4 days with PDGF-BB & IL-1 β , are susceptible to the generation of ROS by PDGF-BB boost (figure 4.4). Further evaluating the limits of the used assay, it is obvious, that a threshold concentration of 200 ng/ml PDGF-BB is required to induce a significant increase in signal over the negative control (0 ng/mL) (figure 4.5). It was further observed, that the signal highly depends on the incubation time. While the trend for each biological repeat is clear, the variance between repeats is almost as high. The assay is working but could greatly benefit from retroactive normalization (figure 4.6) of further optimization towards reproducibility - reducing the required amount of required biological repeats. A potential parameter to explore is the use of different CellROX™ Green concentrations. Finally, a recovery experiment was performed. Before and during the boost, cells were co-incubated with NAC, a potent antioxidant. While not significant after 3 biological repeats, a strong trend was observable, that cells treated with NAC show no CellROX™ Green signal, supporting the expectation that the observed signal is indeed due to the generation of ROS (figure 4.6).

Moreover, it needs to be evaluated if the used PDGF-BB concentration of 200 ng/ml ($\cong 8.25$ nM) is physiologically relevant. Unfortunately, cytokine concentrations are usually assessed as plasma concentrations and no *in vivo* data for local concentrations during paracrine signaling exists. While the manufacturer describes the half maximal effective concentration (EC_{50}) for PDGF-BB-induced proliferation of Balb/c 3T3 cells between 1.0 - 3.0 ng/mL (PeproTech EC Limited, 2022), higher concentrations have frequently been used in the literature. Graves et al. (1996) observed increased formation of cyclic adenosine monophosphate (cAMP) until 10 nM ($\cong 240$ ng/mL) PDGF-BB when assessing the dose-response relationship between cAMP formation after PDGF-BB stimulation of SMCs. Newman et al. (2021b) use 50, nM PDGF-BB for the differentiation of murine VSMCs in the context of atherosclerosis, and Bouzigues et al. (2014) identified 100 ng/mL as a saturating concentration for the generation of H₂O₂ as a response to PDGF-BB signaling in VSMCs.

The next up-and-coming experiment would be the rescue experiment to confirm that the

generation of ROS is indeed caused by PDGF-BB stimulation. Namely by the knockdown of the PDGFR β . The same approach could be pursued to study downstream factors of PDGFR signaling that are involved in the generation of ROS. An exemplary candidate would be STAT1 (STAT1), a TF which deletion reduces plaque formation during atherogenesis and is a required component of PDGF-signaling induced inflammation (He et al., 2015). In addition to its genomic function, it can be imported into mitochondria where it interacts with respiratory complexes and triggers the generation of ROS (Wang et al., 2018a) during hepatic (Lee et al., 2007) and interferon (IFN) induced cancer cell apoptosis (Wang et al., 2018a).

Finally, it has to be addressed, that during the recovery experiment with NAC, the Cell-ROX™ Green signal would multiple times only develop only after cells were taken out of the controlled environment of 37°C and 5 %CO₂. This suggests, that the PDGF-BB is not the sole trigger of ROS generation. To follow up on this idea, it would be beneficial to repeat the experiment under better-controlled conditions. We additionally tried to assess oxidative stress with an anti-8-oxoguanine antibody that detects 8-oxoguanine, a base modification caused by ROS. An attempt that unfortunately failed because the cultivation of HAoSMCs for 7 days in M231 + 1 %FBS was sufficient to induce oxidative damage to the genome (results not shown).

5.3 The GWAS Navigator

Like all primates, humans are extremely visual creatures. We have evolved specialized brain structures for the processing of visual stimuli (Kaas and Balaram, 2014), granting us superior recognition of visual patterns (Mattson, 2014). Thus, making the tools for visualization of data, powerful and important resources for interactive exploration as well as scientific communication.

The GWAS Navigator was developed to display CAD GWAS summary statistics in an easily accessible format for medical researchers. In an iterative process, a multitude of possible implementation approaches was explored, finally arriving at the prototype presented in this thesis. At this point, the tool is built as a bokeh application (section 3.6) that dynamically fetches data from an SQLite database and renders it to the browser.

Databases are a structured collection of data and a staple of data science, providing many advantages over the storage of data in the form of spreadsheets such as access speed, maintainability, and multiuser access. They are designed to hold large collections of data and provide secure and fast access by querying via specifically designed database engines. Relational databases, like SQLite, are the most popular way of flexible representing data in the form of tables with columns and rows. They are usually queried and manipulated with commands using SQL, an internally consistent, human-readable programming language. (Oracle Corporation, 2022a; Oracle Corporation, 2022b) SQLite is a public domain database engine that generates cross-platform, single file databases and is the most used database engine worldwide (The SQLite Consortium, 2022).

While certainly not the only option, bokeh fulfills all the basic requirements for the task at hand. Combining the elegant visualization resources of rendering data with hypertext markup language (HTML), CSS & JS to the browser with the powerful data processing capabilities of python. All bundled into one easy-to-learn ecosystem, providing a level of abstraction that is required for the construction of a prototype. Additionally, the bokeh

server makes the application easily deployable for potential use on a local network (Bokeh Development Team, 2022).

Overall the GWAS Navigator grants a first glance at the genomic context of disease-associated genomic loci. The next step in its development should undoubtedly be the local deployment for the rest of the lab. It provides basic functionality and the possibility for implementation of many additional features. Reaching from basic improvements to usability in the formed tissue-specific annotations to the displayed tracks and the selection tool, to the expansion with new datasets.

5.4 Overlap of CAD Associated Variants with Regulatory Elements is Enriched in Heart, Artery & Lung Tissue

The database makes all the collected not only easily accessible for visualization purposes, but also follow-up studies. The curated data is utilized in an initial postGWAS analysis, scanning for biosamples with cCREs enriched in CAD GWAS variants via Fisher’s exact test. This way identifying 34 biosamples (of [NUMBER] tested) that show significant over-representation (figure 4.12 & table 4.13). After annotation of these biosamples, over 40 % (14/34) of enriched biosamples stem from heart or artery tissue and are therefore directly affected by arteriosclerosis. An additional 20 % stem from lung tissue, an observation in line with the often reported association between heart- and lung disease (Carter et al., 2019; Han et al., 2007). The association of heart- and lung disease prevails even after adjustment for shared risk factors such as tobacco or age. Additionally, Au Yeung et al. (2018) were recently able to demonstrate that greater forced expiratory volume in 1 second (FEV₁) decreases the risk of CAD via Mendelian randomization. Still, the causality of this relationship remains unclear. While it is tempting to speculate that impaired lung function or systematic inflammation by chronic diseases like chronic obstructive pulmonary disease (COPD) result in an elevated risk for cardiovascular diseases, such hypotheses are difficult to evaluate due to reverse causation (Nowak, 2018). CAD might also be the risk factor for lung diseases or both pathologies could share additional not properly adjusted confounding factors. Similarly, the identification of lung tissue in our analysis might hint at the involvement of the lung during the development of CAD or a shared genomic predisposition of heart- and lung disease. Following up on the topic of systemic inflammation, the immune cells in which cCREs enrich are CD14+ monocytes (table ??), a cell type that is known for the secretion of proinflammatory cytokines during injury or inflammation (Kapellos et al., 2019). Interestingly, CD14++CD16+CCR2+ & CD14++CD16-CCR2+ monocytes show significantly higher counts in patients with acute HF over patients with stable HF or CAD (Wrigley et al., 2013).

Finally, the same method and already collected data could be applied to check for the overlap of disease-associated variants with the enhancers identified as part of the ABC model. Further, using the enhancer-promotor connections, to identify potentially affected genes.

Acronyms

24 well multidish	Nunc™Cell-Culture Treated Multidish 24
ABC	activity by contact
API	application programming interface
ATAC-seq	assay for transposase-accessible chromatin using sequencing
ATP	adenosine triphosphate
CAD	coronary artery disease
cAMP	cyclic adenosine monophosphate
cCRE	candidate cis-regulatory element
CNN1	calponin 1
CO₂	carbon dioxide
col I	collagen type I
COPD	chronic obstructive pulmonary disease
Cq	quantification cycle
CRISPR	clustered regularly interspaced short palindromic repeats
CSS	cascading style sheets
CTCF	CCCTC binding factor
dELS	distal enhancer-like elements
DNA	deoxyribonucleic acid
Dock2	dedicator of cytokinesis 2
EC₅₀	half maximal effective concentration
ECAR	extracellular acidification rate
ECM	extracellular matrix
Elk-1	ETS like-1 protein
ENCODE	ENCyclopedia Of DNA Elements project
eQTL	expression quantitative trait loci
ER	entity-relationship
FBS	fetal bovine serum
FCCP	carbonyl cyanide-p-trifluoromethoxyphenylhydrazone
FEV₁	forced expiratory volume in 1 second
FTP	file transfer protocol
GAPDH	glyceraldehyde-3-phosphate dehydrogenase
GESA	gene set enrichment analysis
GI	gastrointestinal
GWAS	genome wide association study
H3K27ac	histone 3 lysine 27 acetylation
H3K4me3	histone 3 lysine 4 trimethylmethionine
H₂O₂	hydrogen peroxide
HAoSMC	human aortic smooth muscle cell
HBSS	Hanks balanced salt solution

HF heart failure
hg19 Genome Reference Consortium Human Build 37
hg38 Genome Reference Consortium Human Build 38
HGNC Human Gene Nomenclature Consortium
HTML hypertext markup language
IFN interferon
IL-1 β interleukin 1 beta
JS javascript
JSON JavaScript Object Notation
KLF4 Kruppel-like factor 4
L2G link to gene
LD lineage disequilibrium
M231 Human Vascular Smooth Muscle Cell Basal Medium (Medium 231)
MAF minor allele frequency
MAP mitogen activated protein
MI myocardial infarction
MMP matrix metalloproteinase
MMP9 matrix metalloproteinase 9
NAC N-acetylcystein
O₂ elemental oxygen
O₂^{•-} superoxide anion radical
OCR oxygen consumption rate
PBS phosphate buffered solution
PCR polymerase chain reaction
PDGF platelet-derived growth
PDGF-BB platelet-derived growth factor-BB
PDGFR platelet-derived growth factor receptor
pELS proximal enhancer-like elements
PI3K phosphatidylinositol 3'-kinase
PIP posterior inclusion probability
PLS promoter-like elements
qPCR quantitative PCR
REST representational state transfer
RNA ribonucleic acid
ROS reactive oxygen species
RT reverse transcription
sc single-cell
Sca1 stem cell antigen-1
SMGS Smooth Muscle Cell Growth Supplement
SNP single nucleotide polymorphism
Sp1 specificity protein 1
SQL structured query language
SRF serum response factor
STAT signal transducers and activators of transcription
STAT1 STAT1
TAD topologically associated domain

TF transcription factor

TGF β transforming Growth Factor beta

TSS transcription start sites

USCS University of California Santa Cruz

VEP variant effect predictor

VSMC vascular smooth muscle cell

WGS whole genome sequencing

Bibliography

Disease Control and Prevention, Centers for (2022). *Heart Disease Facts* / Cdc.Gov. Centers for Disease Control and Prevention. URL: <https://www.cdc.gov/heartdisease/facts.htm> (visited on 06/07/2022).

Fryar, Cheryl D (2012). Prevalence of Uncontrolled Risk Factors for Cardiovascular Disease: United States, 1999–2010, 8.

National Health Service (2017). *Heart Attack*. URL: <https://www.nhs.uk/conditions/heart-attack/> (visited on 06/07/2022).

Montalescot, Gilles et al. (2013). 2013 ESC Guidelines on the Management of Stable Coronary Artery Disease: The Task Force on the Management of Stable Coronary Artery Disease of the European Society of Cardiology. *European Heart Journal* 34, 2949–3003. DOI: [10.1093/eurheartj/ehs296](https://doi.org/10.1093/eurheartj/ehs296).

Tucker, William D., Arora, Yingyot, and Mahajan, Kunal (2022). 1. 1, Treasure Island (FL): StatPearls Publishing.

Yap, Carmen et al. (2021). Six Shades of Vascular Smooth Muscle Cells Illuminated by KLF4 (Krüppel-Like Factor 4). *Arteriosclerosis, Thrombosis, and Vascular Biology*, 41:2693–2707. DOI: [10.1161/ATVBAHA.121.316600](https://doi.org/10.1161/ATVBAHA.121.316600).

Liu, Mingjun and Gomez, Delphine (2019). Smooth Muscle Cell Phenotypic Diversity. *Arteriosclerosis, Thrombosis, and Vascular Biology* 39, 1715–1723. DOI: [10.1161/ATVBAHA.119.312131](https://doi.org/10.1161/ATVBAHA.119.312131).

Grootaert, Mandy O J and Bennett, Martin R (2021). Vascular Smooth Muscle Cells in Atherosclerosis: Time for a Re-Assessment. *Cardiovascular Research* 117, 2326–2339. DOI: [10.1093/cvr/cvab046](https://doi.org/10.1093/cvr/cvab046).

Goumans, Marie-José and Dijke, Peter ten (2018). TGF- Signaling in Control of Cardiovascular Function. *Cold Spring Harbor Perspectives in Biology* 10, a022210. DOI: [10.1101/cshperspect.a022210](https://doi.org/10.1101/cshperspect.a022210).

Batlle, Eduard and Massagué, Joan (2019). Transforming Growth Factor- Signaling in Immunity and Cancer. *Immunity* 50, 924–940. DOI: [10.1016/j.immuni.2019.03.024](https://doi.org/10.1016/j.immuni.2019.03.024).

Davis-Dusenbery, Brandi N. et al. (2011). Down-Regulation of Krüppel-like Factor-4 (KLF4) by MicroRNA-143/145 Is Critical for Modulation of Vascular Smooth Muscle Cell Phenotype by Transforming Growth Factor- and Bone Morphogenetic Protein 4. *The Journal of Biological Chemistry* 286, 28097–28110. DOI: [10.1074/jbc.M111.236950](https://doi.org/10.1074/jbc.M111.236950).

Takahashi, Kazutoshi et al. (2007). Induction of Pluripotent Stem Cells from Adult Human Fibroblasts by Defined Factors. *Cell* *131*, 861–872. DOI: [10.1016/j.cell.2007.11.019](https://doi.org/10.1016/j.cell.2007.11.019).

Pan, Huize et al. (2020). Single-Cell Genomics Reveals a Novel Cell State During Smooth Muscle Cell Phenotypic Switching and Potential Therapeutic Targets for Atherosclerosis in Mouse and Human. *Circulation* *142*, 2060–2075. DOI: [10.1161/CIRCULATIONAHA.120.048378](https://doi.org/10.1161/CIRCULATIONAHA.120.048378).

Chen, Po-Han, Chen, Xiaoyan, and He, Xiaolin (2013). Platelet-Derived Growth Factors and Their Receptors: Structural and Functional Perspectives. *Biochimica et biophysica acta* *1834*, 2176–2186. DOI: [10.1016/j.bbapap.2012.10.015](https://doi.org/10.1016/j.bbapap.2012.10.015).

Heldin, Carl-Henrik (2013). Targeting the PDGF Signaling Pathway in Tumor Treatment. *Cell Communication and Signaling* *11*, 97. DOI: [10.1186/1478-811X-11-97](https://doi.org/10.1186/1478-811X-11-97).

Hu, Weining and Huang, Yu (2015). Targeting the Platelet-Derived Growth Factor Signalling in Cardiovascular Disease. *Clinical and Experimental Pharmacology and Physiology* *42*, 1221–1224. DOI: [10.1111/1440-1681.12478](https://doi.org/10.1111/1440-1681.12478).

Andrae, Johanna, Gallini, Radosa, and Betsholtz, Christer (2008). Role of Platelet-Derived Growth Factors in Physiology and Medicine. *Genes & Development* *22*, 1276–1312. DOI: [10.1101/gad.1653708](https://doi.org/10.1101/gad.1653708).

Levéen, P. et al. (1994). Mice Deficient for PDGF B Show Renal, Cardiovascular, and Hematological Abnormalities. *Genes & Development* *8*, 1875–1887. DOI: [10.1101/gad.8.16.1875](https://doi.org/10.1101/gad.8.16.1875).

Robson, M. C. et al. (1992). Platelet-Derived Growth Factor BB for the Treatment of Chronic Pressure Ulcers. *Lancet (London, England)* *339*, 23–25. DOI: [10.1016/0140-6736\(92\)90143-q](https://doi.org/10.1016/0140-6736(92)90143-q).

Raines, Elaine W (2004). PDGF and Cardiovascular Disease. *Cytokine & growth factor reviews* *15*, 237–254. DOI: [10.1016/j.cytogfr.2004.03.004](https://doi.org/10.1016/j.cytogfr.2004.03.004).

He, Chaoyong et al. (2015). PDGFR Signalling Regulates Local Inflammation and Synergizes with Hypercholesterolaemia to Promote Atherosclerosis. *Nature Communications* *6* (1), 7770. DOI: [10.1038/ncomms8770](https://doi.org/10.1038/ncomms8770).

Newman, Alexandra A. C. et al. (2021a). Multiple Cell Types Contribute to the Atherosclerotic Lesion Fibrous Cap by PDGFR and Bioenergetic Mechanisms. *Nature Metabolism* *3* (2), 166–181. DOI: [10.1038/s42255-020-00338-8](https://doi.org/10.1038/s42255-020-00338-8).

Sies, Helmut and Jones, Dean P. (2020). Reactive Oxygen Species (ROS) as Pleiotropic Physiological Signalling Agents. *Nature Reviews Molecular Cell Biology* *21* (7), 363–383. DOI: [10.1038/s41580-020-0230-3](https://doi.org/10.1038/s41580-020-0230-3).

Nayernia, Zeynab, Jaquet, Vincent, and Krause, Karl-Heinz (2014). New Insights on NOX Enzymes in the Central Nervous System. *Antioxidants & Redox Signaling* *20*, 2815–2837. DOI: [10.1089/ars.2013.5703](https://doi.org/10.1089/ars.2013.5703).

- Sundaresan, M. et al. (1995). Requirement for Generation of H₂O₂ for Platelet-Derived Growth Factor Signal Transduction. *Science (New York, N.Y.)* *270*, 296–299. DOI: [10.1126/science.270.5234.296](https://doi.org/10.1126/science.270.5234.296).
- Bouzigues, Cedric I. et al. (2014). Regulation of the ROS Response Dynamics and Organization to PDGF Motile Stimuli Revealed by Single Nanoparticle Imaging. *Chemistry & Biology* *21*, 647–656. DOI: [10.1016/j.chembiol.2014.02.020](https://doi.org/10.1016/j.chembiol.2014.02.020).
- Uffelmann, Emil et al. (2021). Genome-Wide Association Studies. *Nature Reviews Methods Primers* *1* (1), 1–21. DOI: [10.1038/s43586-021-00056-9](https://doi.org/10.1038/s43586-021-00056-9).
- Flint, Jonathan (2013). GWAS. *Current Biology* *23*, R265–R266. DOI: [10.1016/j.cub.2013.01.040](https://doi.org/10.1016/j.cub.2013.01.040).
- Schaid, Daniel J., Chen, Wenan, and Larson, Nicholas B. (2018). From Genome-Wide Associations to Candidate Causal Variants by Statistical Fine-Mapping. *Nature reviews. Genetics* *19*, 491–504. DOI: [10.1038/s41576-018-0016-z](https://doi.org/10.1038/s41576-018-0016-z).
- Lichou, Florence and Trynka, Gosia (2020). Functional Studies of GWAS Variants Are Gaining Momentum. *Nature Communications* *11*, 6283. DOI: [10.1038/s41467-020-20188-y](https://doi.org/10.1038/s41467-020-20188-y).
- Slatkin, Montgomery (2008). Linkage Disequilibrium — Understanding the Evolutionary Past and Mapping the Medical Future. *Nature reviews. Genetics* *9*, 477–485. DOI: [10.1038/nrg2361](https://doi.org/10.1038/nrg2361).
- Mountjoy, Edward et al. (2021). An Open Approach to Systematically Prioritize Causal Variants and Genes at All Published Human GWAS Trait-Associated Loci. *Nature Genetics* *53* (11), 1527–1533. DOI: [10.1038/s41588-021-00945-5](https://doi.org/10.1038/s41588-021-00945-5).
- Zerbino, Daniel R. et al. (2015). The Ensembl Regulatory Build. *Genome Biology* *16*, 56. DOI: [10.1186/s13059-015-0621-5](https://doi.org/10.1186/s13059-015-0621-5).
- Moore, Jill E. et al. (2020). Expanded Encyclopaedias of DNA Elements in the Human and Mouse Genomes. *Nature* *583* (7818), 699–710. DOI: [10.1038/s41586-020-2493-4](https://doi.org/10.1038/s41586-020-2493-4).
- Buenrostro, Jason D. et al. (2013). Transposition of Native Chromatin for Fast and Sensitive Epigenomic Profiling of Open Chromatin, DNA-binding Proteins and Nucleosome Position. *Nature Methods* *10* (12), 1213–1218. DOI: [10.1038/nmeth.2688](https://doi.org/10.1038/nmeth.2688).
- Buenrostro, Jason D. et al. (2015a). ATAC-seq: A Method for Assaying Chromatin Accessibility Genome-Wide. *Current Protocols in Molecular Biology* *109*, 21.29.1–21.29.9. DOI: [10.1002/0471142727.mb2129s109](https://doi.org/10.1002/0471142727.mb2129s109).
- Buenrostro, Jason D. et al. (2015b). Single-Cell Chromatin Accessibility Reveals Principles of Regulatory Variation. *Nature* *523* (7561), 486–490. DOI: [10.1038/nature14590](https://doi.org/10.1038/nature14590).

- Fulco, Charles P. et al. (2019). Activity-by-Contact Model of Enhancer–Promoter Regulation from Thousands of CRISPR Perturbations. *Nature Genetics* 51 (12), 1664–1669. DOI: [10.1038/s41588-019-0538-0](https://doi.org/10.1038/s41588-019-0538-0).
- Nasser, Joseph et al. (2021). Genome-Wide Enhancer Maps Link Risk Variants to Disease Genes. *Nature* 593 (7858), 238–243. DOI: [10.1038/s41586-021-03446-x](https://doi.org/10.1038/s41586-021-03446-x).
- Lieberman-Aiden, Erez et al. (2009). Comprehensive Mapping of Long-Range Interactions Reveals Folding Principles of the Human Genome. *Science* 326, 289–293. DOI: [10.1126/science.1181369](https://doi.org/10.1126/science.1181369).
- Wit, Elzo de and Laat, Wouter de (2012). A Decade of 3C Technologies: Insights into Nuclear Organization. *Genes & Development* 26, 11–24. DOI: [10.1101/gad.179804.111](https://doi.org/10.1101/gad.179804.111).
- Dixon, Jesse R. et al. (2012). Topological Domains in Mammalian Genomes Identified by Analysis of Chromatin Interactions. *Nature* 485 (7398), 376–380. DOI: [10.1038/nature11082](https://doi.org/10.1038/nature11082).
- Wang, Yanli et al. (2018b). The 3D Genome Browser: A Web-Based Browser for Visualizing 3D Genome Organization and Long-Range Chromatin Interactions. *Genome Biology* 19, 151. DOI: [10.1186/s13059-018-1519-9](https://doi.org/10.1186/s13059-018-1519-9).
- Pombo, Ana and Dillon, Niall (2015). Three-Dimensional Genome Architecture: Players and Mechanisms. *Nature Reviews Molecular Cell Biology* 16 (4), 245–257. DOI: [10.1038/nrm3965](https://doi.org/10.1038/nrm3965).
- Burtenshaw, Denise et al. (2019). Reactive Oxygen Species (ROS), Intimal Thickening, and Subclinical Atherosclerotic Disease. *Frontiers in Cardiovascular Medicine* 6, 89. DOI: [10.3389/fcvm.2019.00089](https://doi.org/10.3389/fcvm.2019.00089).
- Aragam, Krishna G. et al. (2021). Discovery and Systematic Characterization of Risk Variants and Genes for Coronary Artery Disease in over a Million Participants, 2021.05.24.21257377. DOI: [10.1101/2021.05.24.21257377](https://doi.org/10.1101/2021.05.24.21257377).
- Huggett, Jim and Bustin, Stephen A. (2011). Standardisation and Reporting for Nucleic Acid Quantification. *Accreditation and Quality Assurance* 16, 399. DOI: [10.1007/s00769-011-0769-y](https://doi.org/10.1007/s00769-011-0769-y).
- AgilentTechnologies (2022). *How Agilent Seahorse XF Analyzers Work / Agilent*. URL: <https://www.agilent.com/en/products/cell-analysis/how-seahorse-xf-analyzers-work> (visited on 06/05/2022).
- Thermo Fisher Scientific Inc. (2022). *CellROX Green Reagent, for Oxidative Stress Detection*. URL: <https://www.thermofisher.com/order/catalog/product/C10444> (visited on 06/05/2022).
- Newman, Alexandra A. C. et al. (2021b). Multiple Cell Types Contribute to the Atherosclerotic Lesion Fibrous Cap by PDGFR and Bioenergetic Mechanisms. *Nature Metabolism* 3 (2), 166–181. DOI: [10.1038/s42255-020-00338-8](https://doi.org/10.1038/s42255-020-00338-8).

- Bokeh Development Team (2022). *Bokeh: Python Library for Interactive Visualization*.
- Langtangen, Hans Peter and Johansen, Anders E. (2015). *Using Web Frameworks for Scientific Applications*. URL: http://hplgit.github.io/web4sciapps/doc/pub/web4sa_plain_all.html#wf:bokeh:flask (visited on 07/14/2022).
- Tipney, Hannah and Hunter, Lawrence (2010). An Introduction to Effective Use of Enrichment Analysis Software. *Human Genomics* 4, 202. DOI: [10.1186/1479-7364-4-3-202](https://doi.org/10.1186/1479-7364-4-3-202).
- Liu, Yan et al. (2005). Kruppel-like Factor 4 Abrogates Myocardin-induced Activation of Smooth Muscle Gene Expression *. *Journal of Biological Chemistry* 280, 9719–9727. DOI: [10.1074/jbc.M412862200](https://doi.org/10.1074/jbc.M412862200).
- Deaton, Rebecca A., Gan, Qiong, and Owens, Gary K. (2009). Sp1-Dependent Activation of KLF4 Is Required for PDGF-BB-induced Phenotypic Modulation of Smooth Muscle. *American Journal of Physiology. Heart and Circulatory Physiology* 296, H1027–1037. DOI: [10.1152/ajpheart.01230.2008](https://doi.org/10.1152/ajpheart.01230.2008).
- Wang, Zhigao et al. (2004). Myocardin and Ternary Complex Factors Compete for SRF to Control Smooth Muscle Gene Expression. *Nature* 428 (6979), 185–189. DOI: [10.1038/nature02382](https://doi.org/10.1038/nature02382).
- Guo, Xia et al. (2015). Dedicator of Cytokinesis 2, A Novel Regulator for Smooth Muscle Phenotypic Modulation and Vascular Remodeling. *Circulation Research* 116, e71–e80. DOI: [10.1161/CIRCRESAHA.116.305863](https://doi.org/10.1161/CIRCRESAHA.116.305863).
- Long, Xiaochun et al. (2008). Myocardin Is Sufficient for a Smooth Muscle-Like Contractile Phenotype. *Arteriosclerosis, Thrombosis, and Vascular Biology* 28, 1505–1510. DOI: [10.1161/ATVBAHA.108.166066](https://doi.org/10.1161/ATVBAHA.108.166066).
- Owens, Gary K., Kumar, Meena S., and Wamhoff, Brian R. (2004). Molecular Regulation of Vascular Smooth Muscle Cell Differentiation in Development and Disease. *Physiological Reviews* 84, 767–801. DOI: [10.1152/physrev.00041.2003](https://doi.org/10.1152/physrev.00041.2003).
- Dobnikar, Lina et al. (2018). Disease-Relevant Transcriptional Signatures Identified in Individual Smooth Muscle Cells from Healthy Mouse Vessels. *Nature Communications* 9 (1), 4567. DOI: [10.1038/s41467-018-06891-x](https://doi.org/10.1038/s41467-018-06891-x).
- Johnson, Jason L. (2017). Metalloproteinases in Atherosclerosis. *European Journal of Pharmacology* 816, 93–106. DOI: [10.1016/j.ejphar.2017.09.007](https://doi.org/10.1016/j.ejphar.2017.09.007).
- Galis, Z. S. et al. (1994). Increased Expression of Matrix Metalloproteinases and Matrix Degrading Activity in Vulnerable Regions of Human Atherosclerotic Plaques. *The Journal of Clinical Investigation* 94, 2493–2503. DOI: [10.1172/JCI117619](https://doi.org/10.1172/JCI117619).
- Langley, Sarah R. et al. (2017). Extracellular Matrix Proteomics Identifies Molecular Signature of Symptomatic Carotid Plaques. *The Journal of Clinical Investigation* 127, 1546–1560. DOI: [10.1172/JCI86924](https://doi.org/10.1172/JCI86924).

PeproTech EC Limited (2022). *Recombinant Human PDGF-BB*. PeproTech. URL: <https://www.peprotech.com/recombinant-human-pdgf-bb> (visited on 07/14/2022).

Graves, L. M. et al. (1996). Platelet-Derived Growth Factor Stimulates Protein Kinase A through a Mitogen-Activated Protein Kinase-Dependent Pathway in Human Arterial Smooth Muscle Cells. *The Journal of Biological Chemistry* 271, 505–511. DOI: [10.1074/jbc.271.1.505](https://doi.org/10.1074/jbc.271.1.505).

Wang, Yan et al. (2018a). The STAT-ROS Cycle Extends IFN-induced Cancer Cell Apoptosis. *International Journal of Oncology* 52, 305–313. DOI: [10.3892/ijo.2017.4196](https://doi.org/10.3892/ijo.2017.4196).

Lee, Hyun Jung et al. (2007). The Role of STAT1/IRF-1 on Synergistic ROS Production and Loss of Mitochondrial Transmembrane Potential during Hepatic Cell Death Induced by LPS/d-GalN. *Journal of Molecular Biology* 369, 967–984. DOI: [10.1016/j.jmb.2007.03.072](https://doi.org/10.1016/j.jmb.2007.03.072).

Kaas, Jon H and Balaram, Pooja (2014). Current Research on the Organization and Function of the Visual System in Primates. *Eye and Brain* 6 (Suppl 1), 1–4. DOI: [10.2147/EB.S64016](https://doi.org/10.2147/EB.S64016).

Mattson, Mark P. (2014). Superior Pattern Processing Is the Essence of the Evolved Human Brain. *Frontiers in Neuroscience* 8, 265. DOI: [10.3389/fnins.2014.00265](https://doi.org/10.3389/fnins.2014.00265).

Oracle Corporation (2022a). *What Is a Database?* URL: <https://www.oracle.com/database/what-is-database/> (visited on 07/13/2022).

Oracle Corporation (2022b). *What Is a Relational Database / Oracle*. URL: <https://www.oracle.com/database/what-is-a-relational-database/> (visited on 07/13/2022).

The SQLite Consortium (2022). *About SQLite*. URL: <https://www.sqlite.org/about.html> (visited on 07/13/2022).

Carter, Paul et al. (2019). Association of Cardiovascular Disease With Respiratory Disease. *Journal of the American College of Cardiology* 73, 2166–2177. DOI: [10.1016/j.jacc.2018.11.063](https://doi.org/10.1016/j.jacc.2018.11.063).

Han, MeiLan K. et al. (2007). Pulmonary Diseases and the Heart. *Circulation* 116, 2992–3005. DOI: [10.1161/CIRCULATIONAHA.106.685206](https://doi.org/10.1161/CIRCULATIONAHA.106.685206).

Au Yeung, Shiu Lun, Borges, Maria-Carolina, and Lawlor, Debbie A. (2018). Association of Genetic Instrumental Variables for Lung Function on Coronary Artery Disease Risk. *Circulation: Genomic and Precision Medicine* 11, e001952. DOI: [10.1161/CIRCGEN.117.001952](https://doi.org/10.1161/CIRCGEN.117.001952).

Nowak, Christoph (2018). Lung Function and Coronary Artery Disease Risk. *Circulation: Genomic and Precision Medicine* 11, e002137. DOI: [10.1161/CIRCGEN.118.002137](https://doi.org/10.1161/CIRCGEN.118.002137).

Kapellos, Theodore S. et al. (2019). Human Monocyte Subsets and Phenotypes in Major Chronic Inflammatory Diseases. *Frontiers in Immunology* 10.

Wrigley, Benjamin J. et al. (2013). CD14++CD16+ Monocytes in Patients with Acute Ischaemic Heart Failure. *European Journal of Clinical Investigation* 43, 121–130. DOI: [10.1111/eci.12023](https://doi.org/10.1111/eci.12023).